2-2-2016

Synthesis and characterization of lanthanide fluorides for forensic neutron detection

ANTONIO RIVERA

Antonio Carlos Rivera
Candidate

Nanoscience and Microsystems Engineering
Department

This dissertation is approved, and it is acceptable in quality and form for publication:

Approved by the Dissertation Committee:

Dr. Marek Osiński, Chairperson

Dr. Robert Busch

Dr. Adam Hecht

Dr. Igal Brenner

This Page Left Intentionally Blank

Synthesis and Characterization of Lanthanide Fluorides for Forensic Neutron Detection

by

Antonio C. Rivera

B.S. Physics; Optical Sciences and Engineering, University of New Mexico, 2010
M.S. Nanoscience and Microsystems, University of New Mexico, 2012
Doctor of Philosophy Nanoscience and Microsystems Engineering, University of New Mexico 2015

Dissertation

Submitted in partial Fulfilment of the
Requirements for the Degree of

Doctor of Philosophy
Nanoscience and Microsystems Engineering

The University of New Mexico
Albuquerque, NM

December 2015

Dedication

To my wife Jennifer Brown:

She has always known when to cheer me on and when to tell me to get on with myself, even when I was not sure what I needed.

She has been a constant companion throughout this journey.

This is for you my love.

Acknowledgments

I would like to express my gratitude to the following organizations and individuals for their help and support in getting me to this point in my academic life.

Organizations:

I would like to thank The National Science Foundation (NSF), The National Consortium for MAINST Research (NMCR), and The Defense Threat Reduction Agency (DTRA) for their funding and support of the work accomplished within this dissertation.

Then I would like to thank The Center for Integrated Nanotechnologies (CINT), Advanced Materials Laboratory (AML), and University of New Mexico Center for High Technology Materials (CHTM). These centers are not only instrumental to the success of this work, but are a driving force for the future of materials science.

I would also like to thank More Graduate Education at Mountain States Alliance (MGE@MSA), Louis Stokes Alliance for Minority Participation (LSAMP), and Integrating Nanotechnology with Cell Biology and Neuroscience Integrative Graduate Education and Research Traineeship (INCBN IGERT) programs for their support thru fellowships and travel awards.

Individuals:

I would first like to thank my committee, Dr. Robert Busch, Dr. Adam Hecht, and Dr. Igal Brenner for their support, and advice throughout this process.

I would especially like to thank my committee chair Dr. Marek Osiński for his support and teachings which will lead me thru the rest of my career and life.

I would like to thank my research group. This dissertation would not be possible without a dedicated team willing to work together. (Dr. Nathan Withers, Nathaniel Cook, Natasha Glazener, Krishnaprasad Sankar, Leisha Armijo, Dr. John Plumley, Brian Akins, Gloria Medina, Gema Alas, Nicole Triño, Dr. Jose Vargas, Dr. Kate Brandt, Dr. Amber McBride, Darcy Kruse, and Dr. Gennady Smolyakov)

I would like to thank Ken Carpenter, UNM Nuclear Engineering Department.

I would also like to thank the scientists and support staff at CINT (Dr. Sergie Ivanov, Dr. Dale Huber, Dr. Ting S Luk, Dr. Jeremy Wright, and Corey Parsons) for their constant willingness to help with advice and access to resources. Their dedication to serving the scientific community was instrumental in the realization of this dissertation.

I would like to thank Dr. Tim Boyle for access to equipment and resources at the AML facility.

I would like to thank Dr. Ying Bing Jiang and his staff at Earth and Planetary Sciences, for their expertise, guidance and superb maintenance of the TEM imaging facilities.

I would like to thank Heather Armstrong and Linda Bugge. Their unwavering dedication to the students has made this journey possible.

I would like to thank Dr. Laura Crossey for her guidance as a mentor thru the LSAMP program. Her advice and support was instrumental to making this dissertation possible.

I would like to thank the staff at CHTM (Dan Bryant, Beth Fuchs, Steven Wawrzyniec, Douglas Wozniak, Joseph Sadler, Joel Straquadine, Karen Walker, Jannell Vander Grift, Chris Hains, Tamara Martinez, Pat Helles, Stefi Weisburd, Jessica Breckenridge, and Juliet Montoya) for their constant willingness to help overcome obstacles and create and environment second to none for the pursuit of academic success.

I would also like to thank my high school math teacher Paul Trujillo. He taught me that I could achieve anything I put my mind to, and that life should be relished.

I would like to thank my parents Antonio H. Rivera and Lois Rivera for teaching me to follow my own path, and to think for myself. Their constant support and encouragement has led me to this point in my life.

To my children, Michael Brown, James Rivera, John Rivera, and Noah Rivera, all that I do I do for you. May you grow into great men and strive to succeed in all of your endeavors.

I would like to thank the faculty at Infinity High School, Mary Batista, Rebecca Mikkleson, Luke Jaramillo, Daniel Cano, and Kassandra Baca, for their support and encouragement.

For anyone else I may have forgotten, thank you for your time and support.

Synthesis and Characterization of Lanthanide Fluorides for Forensic Neutron Detection

by

Antonio C. Rivera

B.S. Physics, University of New Mexico, 2010
M.S. Nanoscience and Microsystems, University of New Mexico, 2012
Doctor of Philosophy Nanoscience and Microsystems Engineering, University of New Mexico 2015

Abstract

Lanthanide fluorides have many uses, and there is a need for high quality nanocrystals to fill this need. Here, the synthesis and characterization of high quality lanthanide fluorides is presented. In particular, this dissertation focuses on dysprosium fluoride doped with ytterbium, to eventually be used as a forensic and clandestine neutron detector material. There is a need for neutron detectors that have no sensitivity to any other type of radiation and can be used as a forensic tool to go back and look at an event. There is the further requirement that such detectors be hard to detect by those being monitored. To this end, here is proposed that a detector which can exploit the transmutation properties of dysprosium could be used in such an environment. This concept does not require real time monitoring, or electronics to record events, making it an excellent candidate for this application.

Table of Contents

List of Figures

List of Tables

List of Abbreviations:

CHTM – Center for High Technology Materials
CINT – Center for Integrated Nanotechnologies
COD – Crystallography Open Database
DHS – Department of Homeland Security
DNA - Deoxyribonucleic Acid
EDS – Energy dispersive X-ray spectroscopy
HRTEM – High resolution TEM
ICDD - International Center for Diffraction Data
IR - Infrared
Ln – Lanthanide
NA – Natural abundance
NCs – Nanocrystals
NIR – Near infrared
OA – Oleic acid
PMMA – Poly(methyl methacrylate)
PL – Photoluminescence
SWIR – Short-wavelength infrared
TEM – Transmission electron microscopy
UNM – University of New Mexico
UV – Ultraviolet
VIS - Visible
XRD – X-ray diffraction

Types of Radiation Symbols

α – alpha particle (2 neutrons and 2 protons)
γ – gamma ray
n - neutron
p – proton

This Page Left Intentionally Blank

This Page Left Intentionally Blank

Chapter 1

Introduction

This dissertation presents a novel concept for detecting thermal neutrons, using a detector that requires no electronics during the neutron event, allowing for clandestine deployment of the detector, with subsequent interrogation of the detector using optical methods, to forensically determine that a neutron even has occurred. This method of neutron detection has not previously been discussed in the literature, and therefore defines a new venue for research.

1.1. Uses for Lanthanide Containing Nanocrystals

The lanthanide elements (Z = 57 – 71) are a group of elements that share similar chemical properties (Haskin and Frey, 1966) with outer electron configurations composed of 5d and 4f electron shells. This similarity means that the series forms similar crystalline structures and therefore substituting between them in crystalline lattices does not lead to degradation of the overall structure of the crystal.

The demand for high quality lanthanide containing nanocrystals (NCs) is growing, as more and more problems are being solved by exploiting the unique properties of the lanthanide elements, and the way that they act when incorporated into a crystalline lattice. These include the ability to easily incorporate multiple lanthanides at various doping levels, because of their similar chemical properties, and also the similarity of their lattice constants, creating stable crystals that can be implemented in many diverse configurations. Growing these crystals on the nanometer scales allows for even more

flexibility, and uses fewer resources, as the smaller size and larger surface area per gram of crystal allows for the exploitation of the NC properties without the need for larger macroscopic crystals. The smaller size also allows for use in disciplines where it is either infeasible to use a macroscopic crystal, or where it is beneficial to have a small size. The small size scale also lends itself to the creation of optically clear composites, as the size of the NCs is much smaller than the wavelength of light and therefore reduces greatly any scattering that would occur with micron size-particles.

In the medical field, there are many promising uses for lanthanide-containing NCs. Their small size allows them to target, and to be taken in by cells, when properly functionalized with proper proteins (Chatteriee et al., 2008; Chatterjee and Yong, 2008; Liu et al., 2010; Liu and Peng, 2010; Setua et al., 2010; Withers et al., 2011; Naccache et al., 2012; Withers et al., 2012; Withers et al., 2013). As can be seen in the literature presented, those NCs can then be used to deliver drugs, enhance imaging, enhance the cell's susceptibility to radiation or to perform any combination of these tasks to a certain type of cell, while also avoiding uptake and/or interference with cells that are not of interest. The complex magnetic properties of the lanthanides make them excellent candidates for contrast agents in various medical imaging applications (Merbach and Tóth, 2001; Aime et al., 2002; Zhou et al., 2010). The high stopping power of the lanthanides, associated with their high Z, allows them to be used to enhance gamma of X-ray radiation therapy (Chatteriee et al., 2008; Chatterjee and Yong, 2008; Withers et al., 2012; Withers et al., 2013; Xiao et al., 2013).

Lanthanides are also used for radiation detection. On a macro-scale, traditionally lanthanides have been exploited as detector media, because of the large cross section for

either neutrons or gamma/X-rays. Neutron counting has been accomplished by exposing a dysprosium foil to a neutron flux, and then using a Geiger counter, to count the beta decays that result from the transmutation of the dysprosium into holmium (Furetta et al., 1986). Lanthanum bromide has been used as a scintillator medium for radiation detectors also (Van Loef et al., 2002; Menge et al., 2007). This hygroscopic crystal needs to be protected from the environment to keep it from degrading, and there has been an effort to create nanoscale crystals (Rivera et al., 2014) which can then be encapsulated and protected from the environment, making these types of detectors much more durable then current macro-scale crystal based systems. A third method is to insert NCs with a large neutron cross section into dye-loaded polymer based detectors to enhance their ability to detect certain types of radiation. This can be seen by work looking into gadolinium based NCs into polymer scintillators to enhance their sensitivity to neutrons (Akiyama et al., 1993; Czirr et al., 1999; Rivera et al., 2011; Osinski et al., 2015).

This is just a narrow look at a few applications that can be found for lanthanide containing NCs, and there is an ever growing list of applications that can be found in the literature.

1.2. Why Fluoride Nanocrystals?

This dissertation will focus on the promise of using dysprosium fluoride to provide a way to design a clandestine and forensic neutron detector, which is not sensitive to any other type of radiation, such as gamma rays, X-rays, etc. Several compositions of lanthanide nanocrystal were considered before settling on fluorides, including oxides, vanadates and garnets. All four compositions were originally

synthesized, and the decision to use fluorides was based on visual differences between dysprosium fluoride (white) and holmium fluoride (pink). In contrast, the other configurations produced white powders for both dysprosium and holmium containing crystals. The visual difference allows for another method of discriminating between detectors that have been exposed to a neutron flux and those that have not, this difference would require a high fluence of neutrons.

Nanocrystals offer many benefits. The NC size is much smaller than the wavelengths of excitation and emission being studied and therefore cause minimal scattering, allowing for the device to be optically clear. The nanocrystaline size and ability to functionalize their surface chemistry allows us to incorporate them into polymers. This allows them to be made more rugged, protecting the crystalline structure. They can also be encapsulated in carbon based polymers, which gives the added benefit of thermalizing the neutrons.

1.3. Dysprosium Fluoride as a Clandestine and Forensic Neutron Detector

When exposed to a neutron flux, dysprosium-164, with a thermal neutron capture cross section of 2653 barns, captures the neutrons and then undergoes transmutation into holmium-164 (McLaren et al., 1988). Unlike other detection methods, this method is only sensitive to a neutron flux, and therefore does not require the subtraction of signals from other types of radiation. This method also does not require any type of active monitoring, and therefore doesn’t require any type of electronics during the radiation event, making the device harder to detect then a device that requires active monitoring to determine the presence of a neutron flux.

The decision to choose fluorides over oxides, both of which have favorable properties for this research, was made because after synthesis of both types of nanocrystal (NC), it was found that while synthesis of both Dy_2O_3 and Ho_2O_3 produce white powders, the synthesis of DyF_3 produces a white powder, while the synthesis of HoF_3 produces a pink powder. This difference could allow for interrogation based on visual inspection of the devices if they were exposed to either a very high flux of neutron or were exposed over a very long period of time.

1.4. Structure of this Dissertation

In chapter 2 we present some background concerning neutron detection, including a look at current neutron technologies being used and a look at real time detection which utilized dysprosium foils to determine neutron exposure. In chapter 3 we will look at numerical modeling of the neutron dysprosium interactions and modeling of the minimum detectability we can expect from a dysprosium based, clandestine and forensic neutron detector. Next in chapter 4 presents the synthesis of lanthanide fluoride nanocrystals, and discuss the incorporation into polymers, and annealing of powders for maximum emission under optical interrogation. After discussing synthesis, chapter 4 presents the structural characterization of the lanthanide fluoride nanocrystals, showing that we have indeed been able to synthesize high quality nanocrystals. Then in chapter 5 we will discuss neutron experiments that have been conducted, and the absorption characterization of the NCs. Next in chapter 6 we will present photoluminescence data which show that our nanocrystals do indeed have the optical properties, which are needed to distinguish holmium from dysprosium in the lattice. Finally in chapter 7 we will

present our conclusions, and discuss future research that needs to be performed to make a working device possible.

Chapter 2

Background: Neutron Detectors and Neutron Interactions with Dysprosium

2.1 Neutron Interaction with Dysprosium

The basic unit used to describe the nuclear cross section (σ) of an atom is the barn, which is defined as 10^{-28} m^2, and thermal neutron flux Φ is measured in n/cm^2s (McNaught, 1997). In this dissertation, neutron capture of ^{164}Dy (n,γ) nuclei is discussed. This interaction is the capture of a neutron in the nucleus of the dysprosium atom. This interaction leaves the compound nucleus ^{165}Dy in an excited state, which can emit gamma rays as it de-excites. ^{165}Dy is radioactive and decays by β^- emission ($t_{1/2}$ = 2.3 hours) to ^{165}Ho, which is a stable isotope of holmium.

2.2 Current Neutron Detectors

Standard detectors of slow neutrons rely on the $^{10}B(n,\alpha)$, $^{6}Li(n,\alpha)$, or $^{3}He(n,p)$ reactions, neutron capture followed by alpha or proton emission. The thermal neutron cross section for the $^{10}B(n,\alpha)$ reaction is 3840 barns, and the natural abundance of ^{10}B is 19.8%, making it very useful material. The most common detector based on the boron reaction is a BF_3 gas tube. Boron-loaded scintillators are also used, although they encounter the challenge of discriminating between gamma ray backgrounds and gamma ray due to neutrons. The thermal neutron cross section for the $^{6}Li(n,\alpha)$ reaction is 940 barns, and the natural abundance of ^{6}Li is only 7.4%. While very useful, it is not as

effective as ^{10}B. The thermal neutron cross section for the $^{3}He(n,p)$ reaction is 5330 barns, but its natural abundance of only 0.0001%, and the only way to produce it in usable quantities is when enriching weapons grade plutonium, the limited supply resulting in a prohibitively high cost in the past few years.

A dramatic illustration of the need for novel concepts in neutron detection is the recent crisis with the interrupted deployment of 1,300-1,400 ^{3}He neutron detectors (each costing ~$800,000) by the Department of Homeland Security (DHS) (Wald, 2009). After spending $230 million to develop those detectors, with the intent of installing them in ports around the world to monitor possible attempts to smuggle radioactive materials, DHS was forced to stop the deployment due to the shortage of ^{3}He, with the demand exceeding the supply by a factor of 10.

Another example is the need for a detector which could be deployed to detect neutrons, but not give away the geometry of the neutron source, following the START treaty between Russia and the United States (Woolf, 2014). A provision in this treaty states that all ballistic missiles in either arsenal must contain only one warhead. The issue is that the missiles in question can be equipped with one to three warheads. Although it is not difficult to detect whether there are one or three warheads per missile, the catch is that it must be done without giving hints as to the geometry of the warheads contained in the missile. A passive detector could easily be implemented to see the change in flux but not the geometry if properly place on the missile for detection.

In addition to the problems discussed above, some applications may benefit from the ability to do forensic analysis for radioactive events that have occurred (Davidson and

Koppelman, 2008), to determine a chain of custody for the materials, and any event at the time of detection. Materials that transmute into stable isotopes upon capture of a neutron could be used not only to determine the magnitude of the event at the time of the irradiation, but could be revisited at a later time in the event of loss or corruption of data, this would make the chain of custody determination more reliable. Furthermore, materials with these properties could also be deployed as covert detectors, and later recovered to be analyzed to learn if an event happened and what was the magnitude of that event. In the case of dysprosium, if there are isotopic data available for the detector both before and after the event, then not only the magnitude but also the time of exposure, duration of exposure, and the flux of neutrons thru the detector could be determined. This course of action requires very precise knowledge of the state of the detector before and after the event.

2.2.1. Boron Detectors

Boron detectors are based on ^{10}B isotope reactions with neutrons, which result in a ^{7}Li ion, the emission of an alpha particle (α), and 94% of the time a gamma ray (γ) (Siegmund et al., 2007):

$$^{1}n + {}^{10}B \rightarrow {}^{7}Li\ (1.01\ MeV) + \alpha\ (1.8\ MeV)\ 6\%\ \text{of the time or} \quad (3.1)$$

$$^{1}n + {}^{10}B \rightarrow {}^{7}Li\ (0.84\ MeV) + \alpha\ (1.47\ MeV) + \gamma\ (0.48\ MeV)\ 94\%\ \text{of the time} \quad (3.2)$$

Detectors using ^{10}B typically either detect the gamma rays produced in 94% of the events, or look for an electron cascade produced in the detector material by the emitted α particle (Siegmund et al., 2007; McGregor et al., 2008; Lintereur et al., 2009). In both cases the final products, γ and β^-, are produced by other reactions, and therefore

require some type of discrimination method to determine whether or not the event was caused by a neutron. These methods also require constant monitoring by electronics, which make them hard to conceal if placed in situations where there may be a reason for the parties being monitored to want to tamper with or destroy the device.

2.2.2. Lithium Detectors

Lithium detectors are based on ^{6}Li neutron capture, which produces ^{3}H and an alpha particle (Dunning et al., 1935):

$$^{1}n + {}^{6}Li \rightarrow {}^{3}H\ (2.73\ MeV) + \alpha\ (2.05\ MeV) \tag{3.3}$$

Detectors such as the Nucsafe neutron detector (Ely et al., 2009) use a fiber doped with ^{6}Li. When thermal neutrons are absorbed by the lithium, the charged particles produce light in the fiber which can then be detected. Since it is light that is being detected, and not the products directly, the detector is sensitive to both neutrons and gamma rays, making it necessary to use electronics and detector configuration (such as time of flight measurements), to distinguish between gamma rays and neutrons. This detector also relies on electronics to determine the neutron flux, making it harder to conceal in a situation where covert detection is needed.

2.2.3. Helium Detectors

$$^{1}n + {}^{3}He \rightarrow {}^{1}H\ (0.573\ keV) + {}^{3}H\ (0.191\ keV) \tag{3.4}$$

^{3}He has a cross section of 5330 barns for thermal neutrons. The daughter products of the reaction move in opposite directions and produce an output pulse proportional to 0.764 keV (Ricci and Hahn, 1965). This pulse can be detected and distinguished easily

from signals created by gamma rays or other types of ionizing radiation. This makes ^{3}He an ideal detector for thermal neutrons. Because of this, detectors based on ^{3}He are superior to other detectors. The issues involved with these detectors are that they still require electronics to actively monitor the detector to gain a signal from the neutron event. This need for electronics once again makes the detector hard to conceal in a covert situation. Although these detectors are superior to other types, the real issue with helium detectors is the availability and cost of ^{3}He, as discussed above (Wald, 2009).

2.3. Neutron Interactions with Dysprosium

Upon the capture of a thermal neutron, ^{164}Dy can capture a neutron to produce ^{165}Dy which β^- decays to produce ^{165}Ho, or with two neutron captures, ^{164}Dy can become ^{166}Dy and after two β^- decays becomes ^{166}Er, as illustrated in Figure 2.1.

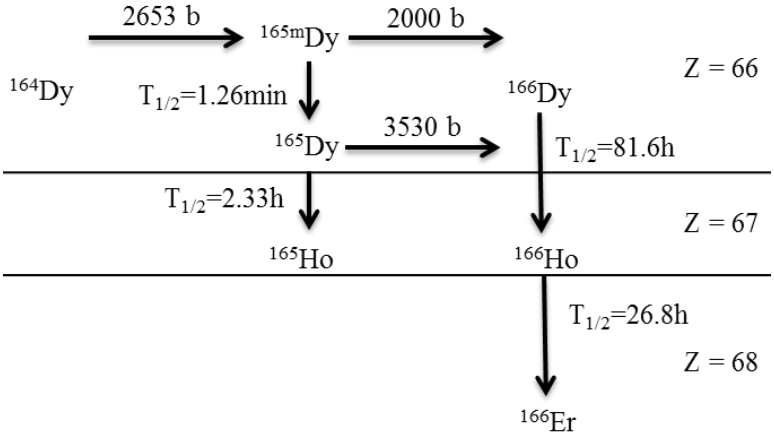

Figure 2.1: Reaction model of ^{164}Dy for neutron capture and β^- decay (McLaren et al., 1988)

The key concept in how to use these processes for optically-enabled neutron detection relies on significant differences in optical properties of Dy, Ho, and Er that are not sensitive to a particular isotope, but change considerably from one element to another.

Thin foils of metallic dysprosium have been in use for slow neutron radiography (Hawkesworth and Walker, 1969), where beta particle emission is used as a means of quantifying the exposure. In our concept, instead of observing the decay events, the same information can be retrieved by optical interrogation of the transmuted elements. This allows deployment of a completely passive detector, which can be examined days or even months after exposure for the presence of neutrons.

The proposed concept should not be confused with long-established luminescence dosimetry methods. These rely on metastable atomic states. By exciting these states the material luminesces. Dysprosium activators have been used in calcium sulfide and calcium fluoride TLDs (Furetta et al., 1986; Yang et al., 2004). The main difference between TLDs and the use of dysprosium, is that TLDs are sensitive to both neutrons and gamma rays, while the proposed detectors will be completely insensitive to gamma irradiation and will provide a very important capability of eliminating the associated false alarms for example with naturally occurring, innocuous gamma sources. To achieve this level of functionality on TLDs, pairs of different detectors have to be used, with one practically insensitive to neutrons, and another one with higher neutron sensitivity (d'Errico and Bos, 2004). This limits the accuracy of the measurements and makes their analysis more complicated. Another important advantage of the proposed sensor is the tamper-proof character of the information stored after exposure. In contrast to TLDs, whose activated trap states can be easily depleted by heating the dosimeter (note that

OSL is even more vulnerable from this point of view, as information can be erased simply by heating), the relative fractions of Dy, Ho, and Er after exposure cannot be manipulated without using a neutron source. Thus, the detector will be very useful if forensic evidence needs to be collected in situations when any suspicion of tampering would need to be eliminated. If desired, unique signatures can be easily introduced into the proposed detectors by adding combinations of nanocrystals (NCs) made of materials with low thermal neutron capture cross sections that could provide optical encoding (fingerprinting) of individual sensors.

While the concept described above applies equally well to bulk materials and to NCs, we believe that the nanocrystaline approach is much more attractive due to its significantly lower cost, relative ease of colloidal synthesis of high quality NCs with controlled composition, and superior optical and mechanical properties of NCs compared to their bulk counterparts. One particular advantage of NCs for neutron detection is that they can be integrated into a transparent polymer host without causing optical scattering, and the host can serve the dual functions of making the neutron detector mechanically robust as well as moderating incoming neutrons, improving the probability of interaction and detection sensitivity.

2.4. Comparison with Other Neutron Captors

To demonstrate that the selection of ^{164}Dy offers the best combination of high thermal neutron cross section, high natural abundance (and hence low cost), and relatively rapid conversion into a chemically compatible stable isotope of a different element than the original target, Tables 2.1 and 2.2 are presented. They show all possible candidate targets

with cross sections higher than that of ^{164}Dy. Only the isotopes that split into smaller fragments as a result of neutron capture have been excluded from Table 1, as fission fragments will have a range much greater than the size the nanocrystals, with considerable damage inflicted upon the NC itself, which would make any quantitative analysis virtually impossible. All cases when the final product is an isotope of the same element as the original target, highlighted in red, are not suitable for simple optical interrogation and would require a much more sophisticated isotope shift analysis. Also highlighted in red are targets with very low natural abundance, which are eliminated from consideration due to their high cost, and targets with short half-lives that are not suitable for long-term monitoring. The otherwise suitable reaction products that are highlighted in yellow are significantly different in their chemical properties compared to the original target element; hence their behavior within NCs, especially at large concentrations, would be problematic. For example, $n + {}^{10}B \rightarrow {}^{6}Li + \alpha$ will lead to decomposition of the NCs because of the difference in lattice structure that boron and lithium create. Boron preferentially forms hexagonal lattice structures, while lithium forms body centered cubic lattice structures. This difference will lead to the crystals quickly developing defects in the structure and decomposition as ^{6}Li is produced. In contrast, all products of ^{164}Dy reactions are lanthanides, fully compatible with the crystalline structure of the original NC. The natural abundance of ^{164}Dy of 28.2% requires no isotopic separation to measure changes in sensor's optical properties using inexpensive equipment. As shown in Figure 2.1 and 2.2, all the naturally occurring isotopes of dysprosium have a path to ^{164}Dy through neutron capture, so with knowledge of the original isotopic make-up of the detector one could determine the time and intensity of the neutron flux experienced by

the detector. This will be discussed further in the mathematical modeling section.

Even though its thermal neutron capture cross section is significantly lower than that of ^{164}Dy, ^{6}Li has been included in Tables 2.1 and 2.2 for comparison purposes, as it is commonly used in neutron detection.

Note that ^{165}Dy has been included in Tables 2.1 and 2.2 for completeness, but in a detector it will only appear as a product of neutron capture by ^{164}Dy. It will, however, play an important role in reconstruction of neutron exposure history.

Target isotope	Cross section [barns]	Natural abundance	Target half-life	Reaction	Reaction product	Product half-life	Final product
Xe-135	2665000	0%	9.14 hours	(n,γ)	Xe-136	Stable	
Gd-157	253000	24.80%	Stable	(n,γ)	Gd-158	Stable	
Gd-155	60700	14.80%	Stable	(n,γ)	Gd-156	Stable	
Sm-149	40520	13.80%	Stable	(n,γ)	Sm-150	Stable	
Gd-153	22300	0%	240 days	(n,γ)	Gd-154	Stable	
Cd-113	20720	12.22%	Stable	(n,γ)	Cd-114	Stable	
Rh-105	15840	0%	35.4 hours	(n,γ)	Rh-106	30 s	Pd-106
Sm-151	15140	0%	90 years	(n,γ)	Sm-152	Stable	
Eu-152	12790	0%	13 years	(n,γ)	Eu-153	Stable	
Eu-151	9184	47.80%	1.7E18 y	(n,γ)	Eu-152	13 years	Sm-152
He-3	5330	0.000137%	Stable	(n,p)	H-3	12.3 year	He-3
B-10	3840	19.80%	Stable	(n,α)	Li-7	Stable	
Eu-155	3760	0%	4.7 years	(n,γ)	Eu-156	15.9 days	Gd-156
Dy-165	3530	0%	2.3 hrs	(n,γ)	Dy-166	81.6 hrs	Er-166
Hg-196	3078	0.15%	Stable	(n,γ)	Hg-197	64 hrs	Au-197
Os-184	3000	0.02%	Stable	(n,γ)	Os-185	94 days	Re-185
Dy-164	2653	28.18%	Stable	(n,γ)	Dy-165	2.3 hrs	Ho-165
Li-6	940	7.59%	Stable	(n,α)	H-3	12.3 yrs	He-3

Table 2.1. Relevant data for isotopes with high thermal neutron cross sections (Sears, 1992; Cutler et al., 2000; Sonzongi, 2009) and their evaluation for neutron detection, sorted by neutron cross-section.

Target isotope	Cross section [barns]	Natural abundance	Target half-life	Reaction	Reaction product	Product half-life	Final product
B-10	3840	19.80%	Stable	(n,α)	Li-7	Stable	
Cd-113	20720	12.22%	Stable	(n,γ)	Cd-114	Stable	
Dy-164	2653	28.18%	Stable	(n,γ)	Dy-165	2.3 hrs	Ho-165
Dy-165	3530	0%	2.3 hrs	(n,γ)	Dy-166	81.6 hrs	Er-166
Eu-151	9184	47.80%	1.7E18 y	(n,γ)	Eu-152	13 years	Sm-152
Eu-152	12790	0%	13 years	(n,γ)	Eu-153	Stable	
Eu-155	3760	0%	4.7 years	(n,γ)	Eu-156	15.9 days	Gd-156
Gd-153	22300	0%	240 days	(n,γ)	Gd-154	Stable	
Gd-155	60700	14.80%	Stable	(n,γ)	Gd-156	Stable	
Gd-157	253000	24.80%	Stable	(n,γ)	Gd-158	Stable	
He-3	5330	0.000137%	Stable	(n,p)	H-3	12.3 year	He-3
Hg-196	3078	0.15%	Stable	(n,γ)	Hg-197	64 hrs	Au-197
Li-6	940	7.59%	Stable	(n,α)	H-3	12.3 yrs	He-3
Os-184	3000	0.02%	Stable	(n,γ)	Os-185	94 days	Re-185
Rh-105	15840	0%	35.4 hours	(n,γ)	Rh-106	30 s	Pd-106
Sm-149	40520	13.80%	Stable	(n,γ)	Sm-150	Stable	
Sm-151	15140	0%	90 years	(n,γ)	Sm-152	Stable	
Xe-135	2665000	0%	9.14 hours	(n,γ)	Xe-136	Stable	

Table 2.2. Relevant data for isotopes with high thermal neutron cross sections (Sears, 1992; Cutler et al., 2000; Sonzongi, 2009) and their evaluation for neutron detection, sorted alphabetically by isotope.

As follows from Table 2.1 and 2.2, ^{164}Dy is the best choice for an isotope that would possess all of the properties needed for the proposed sensor. All other isotopes with larger thermal neutron cross sections have various problems that make them unacceptable for this application. ^{135}Xe is the isotope with the highest thermal neutron cross-section at 2,665,000 barns, but has a half-life of only 9.14 hours, much too short to be useful in a monitoring detector. ^{157}Gd has the highest thermal neutron cross section among all stable elements at 253,000 barns, but upon absorbing a neutron it turns into another stable isotope of gadolinium, ^{158}Gd, making it very difficult to optically distinguish from the original target. While in principle a hyperfine structure of optical spectra can provide information about various isotopes of the same element, those measurements require very

high spectral resolution to detect mass shifts of the order of 100 MHz. In contrast, visual inspection may be sufficient to determine a high level of neutron exposure using the concept described here. ^{151}Eu has the highest natural abundance of 47.8% among all nuclides listed in Table 1, with a reasonably high thermal neutron cross section of 9184 barns, but it transmutes into ^{152}Eu that has a half-life of 13 years, too long for practical purposes.

^{10}B provides a combination of high thermal neutron cross section and high natural abundance very similar to that of ^{164}Dy, and cannot be upfront completely excluded from the list of possible candidate targets. However, the product of ^{10}B decay is ^{7}Li, and at this point we are unaware of any Li compounds that would demonstrate optical activity, as distinct from lanthanide compounds known for their demonstrated optical activity. There is ample experimental evidence (Stouwdam and van Veggel, 2002; Quici et al., 2005; Yang et al., 2008; Wang et al., 2009) that, when inserted in various nano-sized hosts, Dy, Ho, and Er emit light in both visible and near infrared spectral regions, and their emission lines can be easily differentiated.

There are still challenges to overcome with ^{164}Dy as a neutron detector. These include the conversion rate in the current form of DyF_3, using neutron sources available to us, produce a small amount of Ho in the nanocomposites and therefore requires a neutron source with a higher flux of neutrons to create enough Ho to detect in a polymer host. Also the equipment we have been available to us does not have a way to make reproducible results, that can be quantified, and therefore are can only be used to characterize the detectors before and after exposure in a qualitative analysis. Some ways to overcome these issues are to increase the path length through the composite and to

make the measurements more repeatable. These issues will be discussed at length in challenges and future work chapter.

2.5 Conclusion:

Dysprosium-164 is an excellent candidate material for a forensic neutron detector. Unlike other detector configurations there is no need for live monitoring of the material during irradiation. Upon neutron capture ^{164}Dy transmutes through a β^- decay, due to de-excitation, into a stable ^{165}Ho atom which can then be detected days, months or even years after the neutron event occurred. Unlike other methods there is no need to distinguish between neutron events and other types of radiation flux, since this process is only sensitive to a neutron flux, and does not occur with other types of radiation.

Chapter 3

Numerical Modeling of Minimum Detectability and Neutron Interactions with Naturally Occurring Dysprosium Isotopes

First, to determine the minimum amount of holmium that we can detect, a model was built around a Hamamatsu indium antimonide (InSb) infrared detector (Photonics, 2004). The model was built to determine the smallest detectable concentration of holmium in our dysprosium fluoride nanocrystal matrix.

Next, to investigate the potential and the limitations of using naturally occurring dysprosium as a forensic neutron detector, a particular solution to the Bateman equations (Bateman, 1910) is used, to determine the erbium-166, and holmium-165 produced when exposed to a neutron flux. The kinetics of nuclear reactions resulting from the capture of a neutron, resulting from a constant neutron flux, by dysprosium-164 can be described by a set of first-order differential equations as a particular solution to the Bateman equations (Cetnar, 2006). Here this analysis is extended to describe the case of naturally occurring dysprosium, as seen in figure 5.1, which has been synthesized into dysprosium fluoride nanocrystals and packed into a 100% by weight loaded disc with a 2.5 cm diameter and 1 cm thick.

As shown in figure 3.1, all naturally occurring isotopes of dysprosium, upon capture of enough neutrons, eventually feed into ^{164}Dy. ^{160}Dy can capture a neutron to become ^{161}Dy, which can capture a neutron to become ^{162}Dy, which can capture a neutron

to become ^{163}Dy, which can capture a neutron to finally become ^{164}Dy. As all of these isotopes are stable, there is no rate requirement for this process.

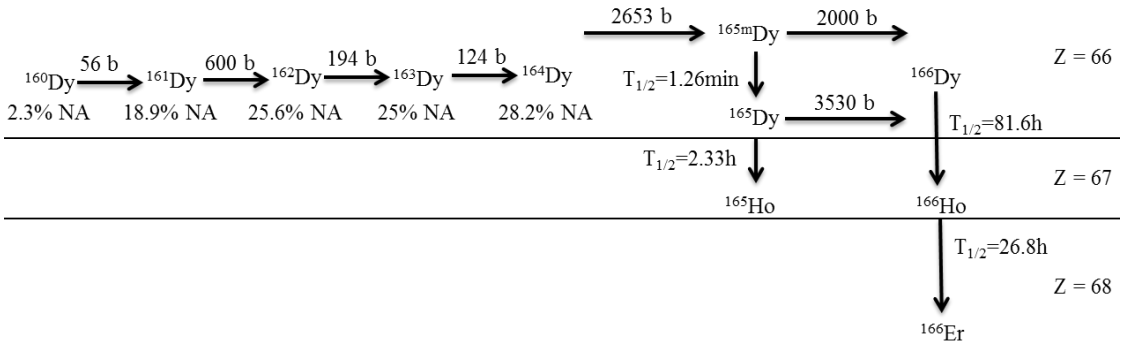

Figure 3.1: Full decay model for naturally occurring dysprosium, including natural abundance (NA) of each dysprosium isotope.

3.1 Minimum Detectability

To determine the minimum photon flux needed by the detector, we use the formula for specific detectivity (formula 3.1) along with data about the detector from Hamamatsu (table 3.1) to determine the photon flux needed by the InSb detector for us to see the emission from the holmium inside of the neutron detector. Using these numbers we are able to determine the minimum flux required, for holmium detection using InSb. This model gives us a minimum flux Q = 2.71 x 10^{17} photons/cm^{2}s, needed to obtain a signal from the detector.

$$D = \frac{\lambda\sqrt{\eta}}{2*hc\sqrt{Q}} \qquad (3.1)$$

Constant	Symbol	Value
Specific Detectivity	D	10^{11} cmHz$^{1/2}$/W
Wavelength	λ	2.1 μm
Quantum Efficiency	η	70%
Plank's Constant	h	6.62 x 10^{-30} cm^{2}kg/s
Speed of Light	c	2.99 x 10^{10} cm/s

Table 3.1: Constants used for specific detectivity formula

Next we take the minimum flux, the formula for intensity absorbed (formula 3.2), and a quantum efficiency (QE) of 70% for holmium fluoride nanocrystals (the QE used is based on measurements taken by (Allain et al., 1991)). We also assume that the disc is placed into an optical system (figure 3.2) which includes a resonator so that we can achieve a 100 cm path length and a lens that can concentrate all of the 2.1 μm emission onto a 1 cm^3 spot (table 3.2). Using this information, the model gives a minimum of 9.679 x 10^{18} atoms/cm^3 needed to be detectable using Hamamatsu's InSb detector. This number is used in the next section to determine the minimum neutron flux that can be detected.

$$I_{abs} = N \cdot \sigma_a \cdot I_{in} \cdot \Delta x \quad (3.2)$$

Constant	Symbol	Value
Absorption Cross Section	σ_a	3 x 10^{-21} cm^2
Path Length	Δx	100 cm
Excitation Intensity	I_{in}	4 x 10^{-4} W/cm^2

Table 3.2: Constants used for intensity absorbed formula.

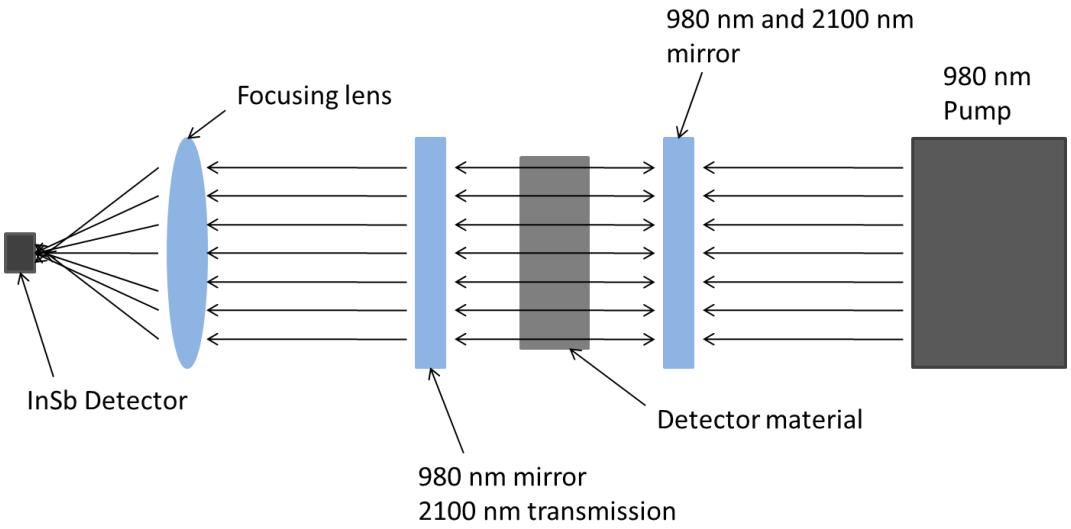

Figure 3.2: Simplified diagram of optical system being modeled.

3.2 Thermal Neutron Irradiation

The kinetics of nuclear reactions resulting from exposure of all naturally occurring dysprosium isotopes due to a constant thermal neutron flux Φ (in $cm^{-2}s^{-1}$) can be described by the following set of differential equations 3.3, in which σ denotes the thermal neutron capture cross section, ϕ denotes the neutron flux, C is the concentration of atoms per cm^2, and λ is the half-life, of the corresponding isotope.

$$dC_{160Dy}/dt = -\sigma_{160Dy}\,\phi\, C_{160Dy}$$

$$dC_{161Dy}/dt = \sigma_{160Dy}\,\phi\, C_{160Dy} - \sigma_{161Dy}\,\phi\, C_{161Dy}$$

$$dC_{162Dy}/dt = \sigma_{161Dy}\,\phi\, C_{161Dy} - \sigma_{162Dy}\,\phi\, C_{162Dy}$$

$$dC_{163Dy}/dt = \sigma_{162Dy}\,\phi\, C_{162Dy} - \sigma_{163Dy}\,\phi\, C_{163Dy}$$

$$dC_{164Dy}/dt = \sigma_{163Dy}\phi\, C_{163Dy} - \sigma_{164Dy}\phi\, C_{164Dy}$$

$$dC_{165mDy}/dt = \sigma_{164Dy}\phi\, C_{164Dy} - \sigma_{165mDy}\phi\, C_{165mDy} - \lambda_{165mDy}\, C_{165mDy} \qquad (3.3)$$

$$dC_{165Dy}/dt = -\sigma_{165Dy}\phi\, C_{165Dy} - \lambda_{165Dy}\, C_{165Dy} + \lambda_{165mDy}\, C_{165mDy}$$

$$dC_{166Dy}/dt = \sigma_{165mDy}\phi\, C_{165mDy} + \sigma_{165Dy}\phi\, C_{165Dy} - \lambda_{166Dy}\, C_{166Dy}$$

$$dC_{165Ho}/dt = -\sigma_{165Ho}\phi\, C_{165Ho} + \lambda_{165Dy}\, C_{165Dy}$$

$$dC_{166Ho}/dt = \sigma_{165Ho}\phi\, C_{165Ho} - \lambda_{166Ho}\, C_{166Ho} + \lambda_{166Dy}\, C_{166Dy}$$

$$dC_{166Er}/dt = \lambda_{166Ho}\, C_{166Ho}$$

The system of linear differential equations with constant coefficients (3.3) allows for analytical solutions, for which the general solution is,

$$y_i = C_{i1}e^{r1t} + C_{i2}e^{r2t} + C_{i3}e^{r3t} + C_{i4}e^{r4t} + C_{i5}e^{r5t} + C_{i6}e^{r6t} + C_{i7}e^{r7t} + C_{i8}e^{r8t} + C_{i9}e^{r9t} + C_{i10}e^{r10t} + C_{i11}e^{r11t};\ i = 1\ldots,11 \qquad (3.4)$$

where exponents r_i ($i = 1\ldots11$) are roots of the characteristic equation of the system of the equations (3.3), and the unknown coefficients C_{ik} are determined from the initial conditions.

The kinetic equations (3.3) are then solved analytically, and then evaluated numerically. A number of cases of interest can be investigated using constants listed in table 3.1, and varying the thermal neutron flux (ϕ) between 1×10^5 n/cm^{3}s and 1×10^{10} n/cm^{3}s, based on the minimum detectability model. The loading of dysprosium atoms in the scintillator material used for calculations is 1.62×10^{26} atoms/cm^3. A time frame of 7

days under constant irradiation is used, and is based on the average time for a container ship to sail across the Atlantic Ocean (Vernimmen et al., 2007).

Isotope	Natural Abundance	Thermal Neutron Cross Section (σ)	Decay Rates (λ)
Dy-160	2.30%	56 barns	Stable
Dy-161	18.90%	600 barns	Stable
Dy-162	25.60%	194 barns	Stable
Dy-163	25.00%	124 barns	Stable
Dy-164	28.20%	2653 barns	Stable
Dy-165	0%	3530 barns	$8.2518 \times 10^{-5} s^{-1}$
Dy-165m	0%	2000 barns	$9.168613 \times 10^{-3} s^{-1}$
Dy-166	0%	N/A	$2.36 \times 10^{-3} s^{-1}$
Ho-165	N/A	64 barns	Stable
Ho-166	0%	N/A	$7.184 \times 10^{-6} s^{-1}$

Table 3.3. Constant parameters used for mathematical model (Firestone, 2000).

3.3 Post Irradiation

After irradiation, the concentration of the stable end products ^{165}Ho and ^{166}Er will continue to change due to the half-life of their parent nuclei created during irradiation. These end products will reach a state where the feed in rate becomes negligible, and the quantities of Ho and Er become very close to their final values.

The post-irradiation kinetics can be described by a reduced system of six first-order differential equations that follow from (3.4) by making the flux $\phi = 0$ in all terms. Therefore we have:

$$dC_{160Dy}/dt = dC_{161Dy}/dt = dC_{162Dy} = dC_{163Dy}/dt = dC_{164Dy}/dt = 0 \qquad (3.5)$$

These equations then lead to the system of equations for post irradiation (3.6):

$$dC_{165mDy}/dt = -\lambda_{165mDy} C_{165mDy}$$

$$dC_{165Dy}/dt = -\lambda_{165Dy} C_{165Dy} + \lambda_{165mDy} C_{165mDy}$$

$$dC_{166Dy}/dt = -\lambda_{166Dy} C_{166Dy}$$

$$dC_{165Ho}/dt = \lambda_{165Dy} C_{165Dy} \qquad (3.6)$$

$$dC_{166Ho}/dt = -\lambda_{166Ho} C_{166Ho} + \lambda_{166Dy} C_{166Dy}$$

$$dC_{166Er}/dt = \lambda_{166Ho} C_{166Ho}$$

Given these equations, the concentrations of each of the involved isotopes can be analyzed after the neutron flux has been removed, and allow us to determine information about the irradiation. Depending on the accuracy with which the isotropic information can be determined, many other characteristics of the irradiation can be determined. For this model the de-excitation due to β^- decay and production of holmium is the focus. Other modes will be left for future research as these are not realistic for measurement in the near future.

3.4 Modeling

Graphical data produced by the mathematical model is presented using the constants and variables discussed in section 3.2 and formulas (3.4) and (3.6) from sections 3.2 and 3.3 above. The loading of dysprosium atoms is 1.62×10^{26} atoms/cm^3. The time duration of the irradiation is 7 days. This time is based on the average time it

takes a shipping container to cross the Atlantic Ocean. All other constants are as describe in section 3.2 above.

3.4.1. During Irradiation

Figures 3.3 and 3.4 show the production of both ^{165}Ho and ^{166}Er during irradiation at varying levels of neutron flux. The graphs are produced by solving the equations in formula (3.4) above for the change in concentration, and plotting the total concentration of ^{165}Ho and ^{166}Er vs. time. In each graph presented in this chapter, there is a horizontal purple line which represents the minimum detectability as calculated in section 3.1. The graphs show that after approximately one day the production rate begins to level off and follow a more linear curve on a log scale, meaning exponential growth, all the way through the 7 day mark.

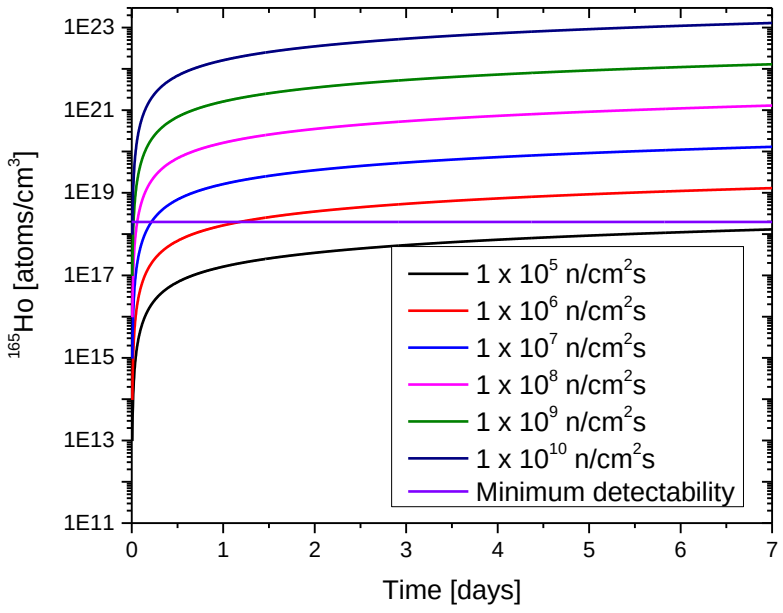

Figure 3.3: Production of ^{165}Ho atoms during neutron exposure.

In the case of ^{165}Ho production during radiation (figure 3.3), at all concentrations between 1 x 10^6 n/cm^{2}s and 1 x 10^{10} n/cm^{2}s, the concentration of ^{165}Ho atoms exceeds the minimum detectability after 1.5 days. At a flux of 1 x 10^5 n/cm^{2}s, the concentration doesn't make it to the minimum detectability line. This tell us that, even if the duration of the neutron flux is present for more than 1.5 days, we will still be able to detect the holmium in the detectors.

In the case of ^{166}Er production (figure 3.4), the graphs show that when the neutron flux is between 1 x 10^5 n/cm^{2}s and 1 x 10^9 n/cm^{2}s, the concentration of ^{166}Er does not cross the minimum detectability line during the 7 day time period. Meanwhile for a neutron flux of 1 x 10^{10} n/cm^{2}s, the concentration does cross the minimum detectability line around day 5. This shows that with higher fluxes, there is a reasonable expectation that even the erbium, in the device could be detected.

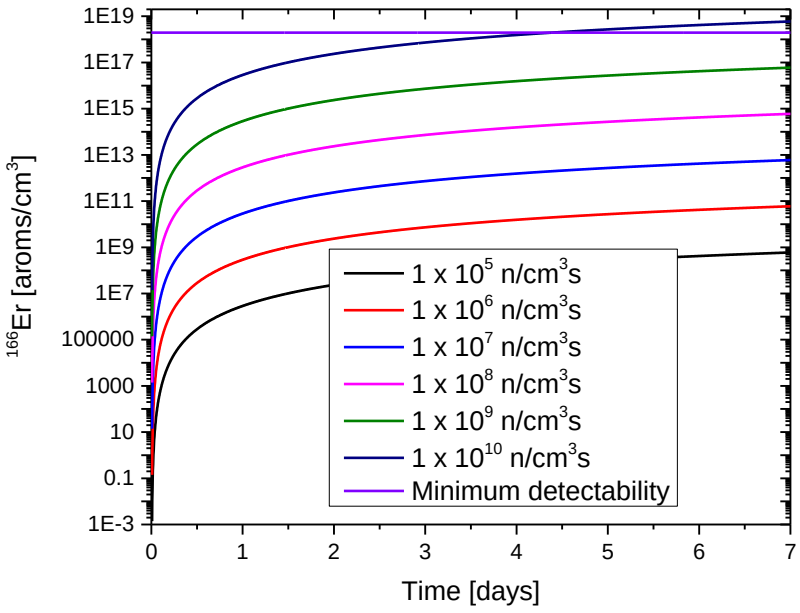

Figure 3.4: Production of ^{166}Er atoms during neutron exposure.

3.4.2. Post Irradiation

Figures 3.5 and 3.6 show how the detector responds after the neutron flux stops, using the kinetic equations described in formula (3.7). Once again solving for the change in concentration, and plotting the total concentration of ^{165}Ho and ^{166}Er vs time. The model is started with the ending numbers from the calculations made for the sample during irradiation. Therefore the zero point for this calculation is at seven days, and the model is run for three days past irradiation.

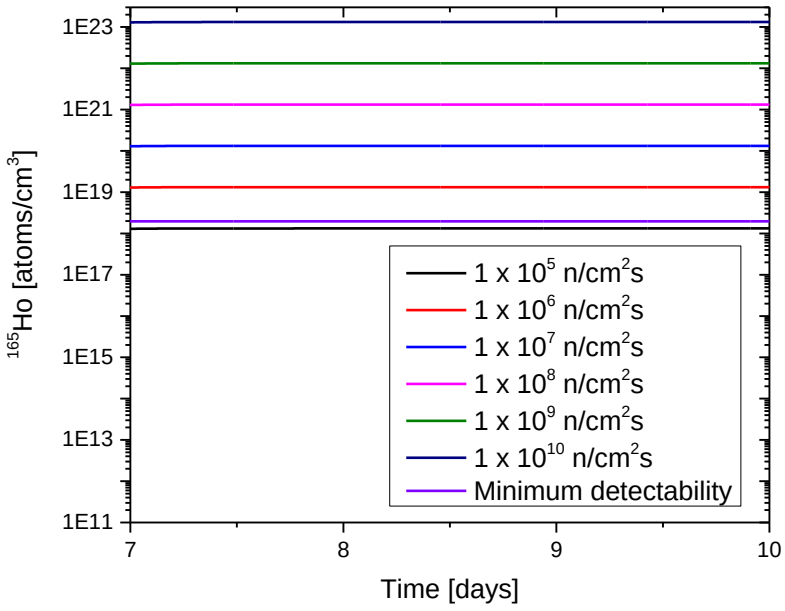

Figure 3.5: ^{165}Ho concentration post neutron exposure.

In the case of ^{165}Ho, the model shows that after irradiation there is very little change in the concentration, after the flux of neutrons stops. This is due to the short half-lives of the constituent isotopes in this branch of the reaction. From this we can see that as soon as the neutron flux is stopped, the concentration of ^{165}Ho is stable.

In the case of ^{166}Er, the model shows that the ^{166}Er branch of the reaction takes longer to reach a steady state, and in the graph the slight positive slope can be seen. This is due to the longer decay times involved with this branch of the reaction. This time is dependent on the transition ^{166}Dy → ^{166}Ho, which has a half-life of 81.6 hours. This half-life dominates the reaction and explains the longer time to reach a steady state.

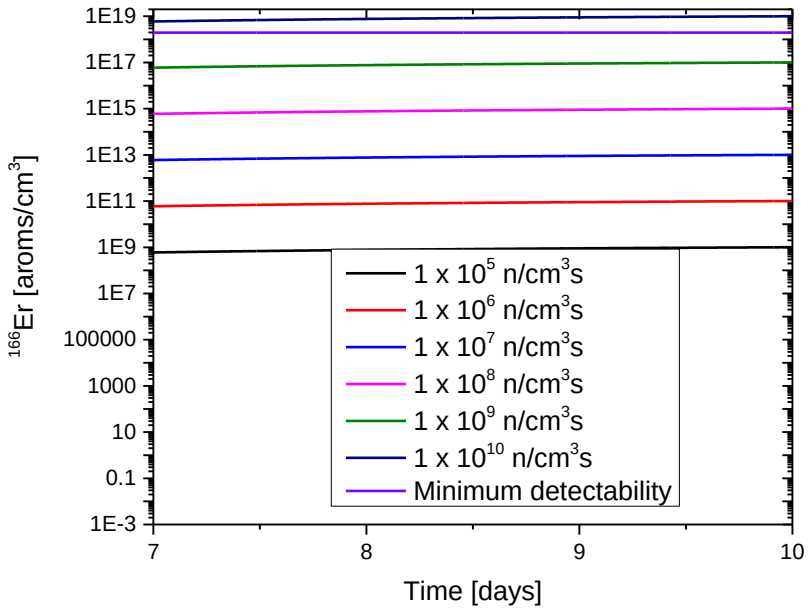

Figure 3.6: ^{166}Er concentration post neutron exposure.

3.4.3. Overall Effect

The two data sets can then be combined to show the overall change in concentration over the full time discussed in this model (figures 3.7 and 3.8). As built the model shows that there is a smooth progression with a quick build up over approximately the first one and a half days. Then as the irradiation continues, the slope becomes more linear on a log scale. Next, after the neutron flux stops, the concentration of ^{165}Ho very quickly reaches a steady state, while the concentration of ^{166}Er continues to increase. This is expected given the differences in the half-lives of the two legs of the reaction.

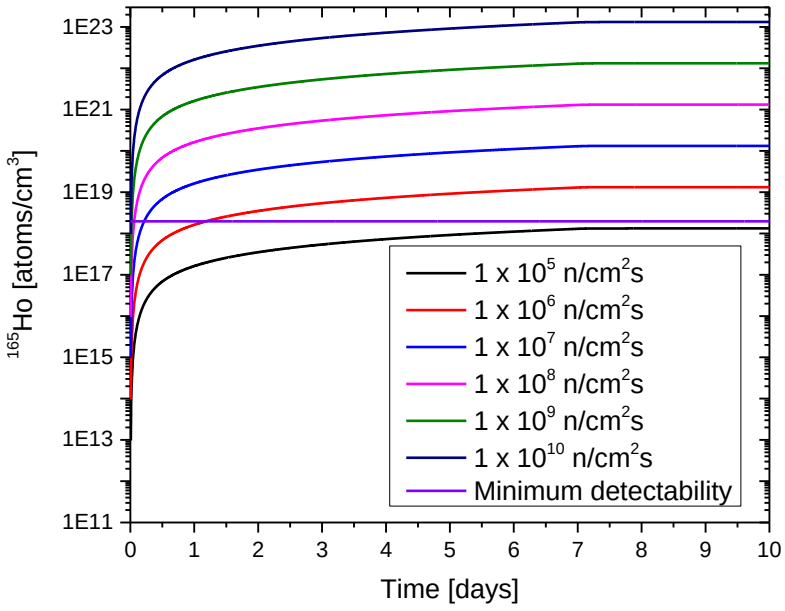

Figure 3.7: ^{165}Ho produced both during and post neutron irradiation.

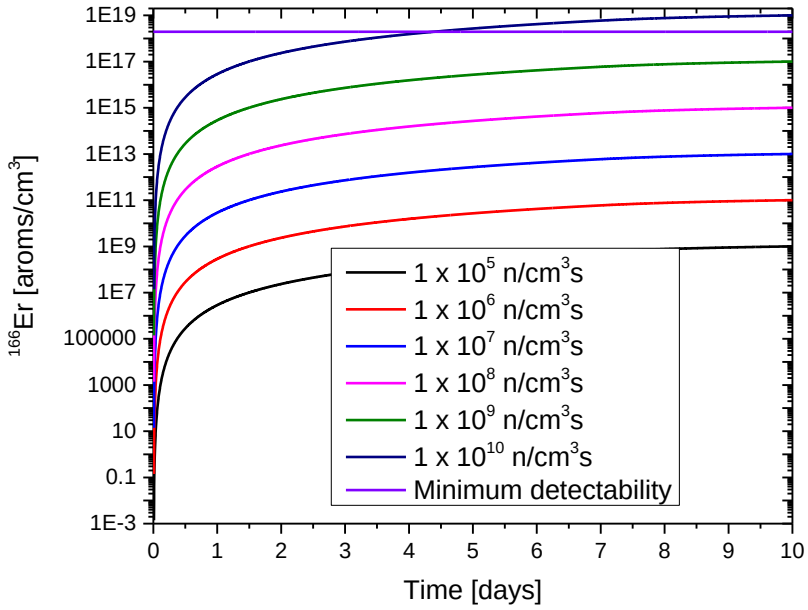

Figure 3.8: ^{166}Er produced both during and post neutron irradiation.

3.5. Conclusion

The Bateman equations based modeling along with the analysis of the minimum detectability, shows that when the dysprosium loaded neutron detector is exposed to a neutron flux of at least 1 x 10^6 n/cm^2s, the ^{165}Ho can be detected. The model also shows the production of ^{166}Er to be within the range of minimum detectability, with a flux of at least 1 x 10^{10} n/cm^2. The model also shows that ^{165}Ho almost instantly reaches a steady concentration, while ^{166}Er takes longer to reach this steady state because of the longer half-life associated with the ^{166}Dy $\rightarrow$ ^{166}Ho transition.

Chapter 4

Synthesis of Lanthanide Fluoride Nanocrystals

4.1. Co-Precipitation Method of Synthesis

To synthesize lanthanide fluoride nanocrystals (NCs), a co-precipitation method was used, as described in Dean's Analytical Chemistry Handbook (Patnaik, 2004). A co-precipitation synthesis is one where the precursors are soluble in the solvent while the products are not. This leads to a very efficient way of building nanocrystals as the precursors have and energy advantage for forming crystals. The methods employed below were all derived from (Withers et al., 2010). For our purposes, there were two different configurations synthesized and studied for this dissertation uncoated, and oleic-acid-coated lanthanide fluorides. The chemical equation which describes this process is listed below:

$$CH_3OH + 1\ mmol\ Ln(NO_3)_3 \bullet 5H_2O + 3\ mmol\ NH_4F$$

$$\rightarrow CH_3OH + 3\ mmol\ NH_4NO_3 + 1\ mmol\ LnF_3/OH + 5H_2O$$

4.2. Laboratory Setup

The setup in the laboratory is conducive to the synthesis of nano-scale particles. There are two chemical hoods, one with a schlenk line (figure 4.1), which allows for synthesis under vacuum or inert gas flow, either nitrogen or argon. There is also an MBraun glove box (figure 4.2) that not only allows for the storage of air sensitive chemicals, it also allows for chemistry to be done in a water and oxygen free

environment. The glove box can be kept under either nitrogen or argon gas and keeps the air in the box at 0.1 ppm H_2O and 0.1 ppm O_2. During synthesis temperature is controlled using a J-KEM Scientific Apollo temperature controller (figure 4.3), which allows for regulated heating of reactants during synthesis. There is also a Carbolite (figure 4.4) oven which allows for heating of samples up to 750 ºC for drying or annealing of samples as well as heating of reactants prior to synthesis. The schlenk line also allows for the attachment of condensers (figure 4.5) which allows for running synthesis under reflux conditions for optimal nucleation.

Figure 4.1: Schlenk line

Figure 4.2: MBraun UNIlab Glove Box

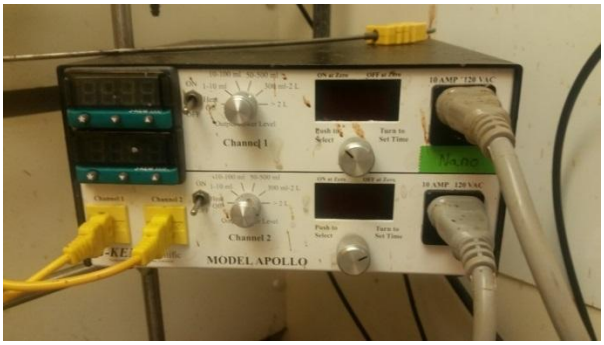

Figure 4.3: J-KEM Scientific Apollo Model Temperature Controller

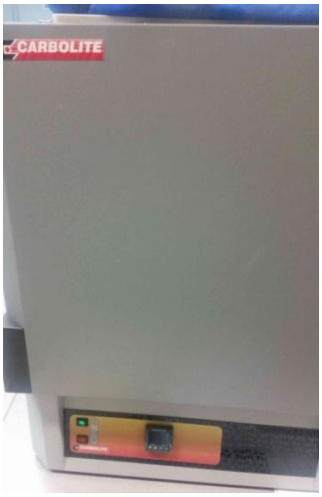

Figure 4.4: Carbolite oven

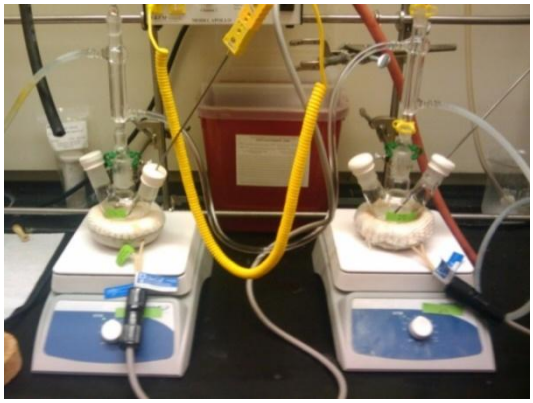

Figure 4.5: LnF_3 synthesis standard setup

4.3. Colloidal Synthesis of LnF_3 NCs

To produce hydroxyl coated lanthanide fluoride nanocrystals, we begin with 35 mL of 1.6 M NH_4F in methanol which is heated to 60 ºC in a three neck flask (figure 4.5). Once the solution reaches 60 ºC we add 2 ml of 1.5 M $Ln(NO_3)_3 \bullet H_2O$. The solution, in the three neck flask, is then allowed to reflux for two hours at 60 ºC. After two hours the solution is allowed to dry, and then the nanocrystals are either annealed to fix the crystalline structure in a powder, or coated with oleic acid so that they are stable in toluene and then able to be incorporated into polymer matrices.

4.3.1. Annealing of Lanthanide Fluoride Nanocrystals

To obtain a powder, which we are able to either incorporate into a KBr matrix, or to use as a powder, the solution is first removed from the cooled three neck flask and added to an alumina crucible and put in an oven at 66 ºC for 4 hours, this removes the methanol, and a powder is collected. In the case of dysprosium fluoride this is a white powder, and for holmium fluoride a pink powder. The powder can be used as is or

annealed at 700 ºC to 1200 ºC (depending on which lanthanide is being synthesized) to enhance the photoluminescence emission. In the case of dysprosium and holmium 1200 ºC is needed to anneal the nanocrystals and enhance their photoluminescent properties. The nanocrystals are then either used as a powder or can be incorporated into a potassium bromide (KBr) matrix.

4.3.2. Synthesis with Lanthanide Fluoride Nanocrystals Coated with Oleic Acid

To obtain nanocrystals coated with oleic acid, we add 0.5 mL of oleic acid to the solution as it cools in the three neck flask. After the solution cools it is passed thru a 2 μm filter to remove any larger particles created during synthesis. The solution is put into a scintillation vial, and is then dried in the oven at 66 ºC for 4 hours and a thick solution is collected. This solution is the nanocrystals in oleic acid, which is not evaporated at 66 ºC. Finally toluene is added to the vial and can be stored in this way until they are incorporated into a PMMA matrix or characterized as a liquid sample.

4.4. Potassium Bromide Pressing

KBr is often used to create infrared transparent optics components, and can be loaded with powders so that they can be interrogated using coherent infrared light. To produce a lanthanide fluoride loaded disc of KBr, KBr powder is mixed with the annealed nanocrystals produced in section 4.3.1. We are able to load KBr with a 2% weight loading of nanocrystals, any higher loading results in the KBr disc falling apart after pressing. The powder is then put into a pneumatic press at 10 tons per square inch for 20 minutes, and a disc is produced which can then be characterized. Although the infrared properties of KBr are favorable for our research, they are also very brittle and

hygroscopic making them less rugged then loaded polymers, and the low weight loading makes them less sensitive if used as a detector.

4.5. Synthesis of Nanocomposites in Poly-Methyl Methacrylate (PMMA)

Poly-methyl Methacrylate (PMMA) was used because it is considered an infrared transparent polymer, it was later abandoned because of a resonance which is around the 2.1 μm emission that we are interested in. To produce PMMA loaded with lanthanide fluoride nanocrystals we first remove the monomethyl ether hydroquine (MEHQ) inhibitor, which is attached to the methacrylate (MMA) to prevent polymerization during shipping, by passing the solution thru a distillation column. We then add the activator azobisisobutyronitrile (AIBN), in differing amounts based on NC loading, as the NCs also act as an activator, to start the polymerization of the solution. The solution is then heated to 90 ºC and monitored at 15 minute increments until the solution is polymerized. At the 15 minute increments the solution is also slowly agitated to remove bubbles. Because of limitations in our setup a 3.7% weight loading was the highest achievable loading in our lab, this is because of the bubbles produced during the polymerization process which we were unable to agitate out at higher weight loadings. This bubbling can be easily controlled in a vacuum oven and therefore allow for much higher weight loading of polymers.

4.4. Conclusion

For all three syntheses presented, molar ratios were used to modify the synthesis for different lanthanide constituents. For this research, the following lanthanide fluorides were synthesized and characterized; DyF_3, HoF_3, DyF_3:10%Yb, HoF_3:10%Yb,

HoF_3:10%Ce, DyF_3:10%Ho DyF_3:10%Ce, and DyF_3:10%Ce10%Ho. We were also able to load our nanocrystals into KBr, and PMMA matrices. The characterization and results of these syntheses, and loadings will be presented in the following chapters.

Chapter 5

Physical Characterization of Lanthanide Fluoride Nanocrystals for Clandestine Neutron Detection

Here we present the physical characterization of lanthanide fluorides, synthesized to be used for clandestine neutron detection and neutron event forensics. The methods to be presented are TEM, XRD, DLS, and zeta-potential. These methods allow us to determine the size, shape, crystallinity, and chemical make-up of our nanocrystals.

5.1. Structural Characterization Equipment

5.1.1. Transmission Electron Microscopy (TEM)

Figure 5.1: JEOL 2010 HRTEM

To obtain images and energy dispersive X-ray spectroscopy (EDS) of the NCs synthesized for this dissertation, a JEOL 2010 high resolution TEM (HRTEM) (figure 5.1) with an Oxford Labs EDS detector was used. The microscope operates at an

acceleration voltage of 210 kV, and is used to obtain images up to 400,000 times magnification. At this resolution it is possible to look at the crystal lattice of the NCs, and to determine their lattice spacing as well as their crystallographic structure.

5.1.2. Energy Dispersive X-Ray Spectroscopy (EDS)

EDS uses secondary X-rays produced from the interaction of the electron beam in the TEM (figure 5.1), and inner shell electron in the atoms contained in the sample. Since the samples are prepared on a copper coated carbon sample grid and with an iron holder these elements are also present in the analysis and can be assumed to be part of the apparatus and not the sample. The method is used to confirm the elemental make-up of the samples but is not accurate enough to give a stoichiometric analysis for the lattice structure (using XRD and HRTEM), optical emission and absorption can also be used to match to literature to determine the phase of the NCs.

5.1.3. X-Ray Diffraction (XRD)

Powder XRD is another method used to determine the lattice structure of the NCs. A Rigaku Smart LAB XRD (figure 5.2) housed at Sandia Labs CINT facility was utilized for this analysis. This method uses an X-ray beam of known wavelength to determine the lattice of the NCs. The X-ray beam interacts with the lattice of the NCs and there is constructive interference creating a diffraction maximum when the lattice constant, angle between the X-ray source theta, and detector, and wavelength of the X-rays lambda satisfy the Bragg equation (Bragg and Bragg, 1913) (5.1):

$$n \bullet \lambda = 2 \bullet d \bullet \sin(\theta) \tag{5.1}$$

The intensity as a function of angle is recorded by the diffractometer to analyze the lattice constants in the material. If the material is known the data can then be matched to either the Crystallography Open Database (COD) (Downs and Hall-Wallace, 2003; Gražulis et al., 2009; Gražulis et al., 2012), or the International Center for Diffraction Data (ICCD) database (Faber and Fawcett, 2002; Fawcett et al., 2009).

Figure 5.2: Rigaku Smart LAB XRD

5.1.4. Dynamic Light Scattering (DLS)

A Wyatt Technology DynaPro Titan dynamic light scattering (DLS) device (figure 5.3), was used to determine the hydrodynamic size of the nanocrystals. This method uses a laser to determine the velocity due to Brownian motion of the particles in a liquid solution. This measurement along with the viscosity of the liquid allows for the determination of the hydrodynamic size of the particles. This method is able to probe the sample and look at a large number of particles, and is therefore able to give a more accurate size distribution then can be obtained thru TEM analysis.

Figure 5.3: Wyatt Technologies DynaPro Titan DLS

5.1.5. Zeta Potential

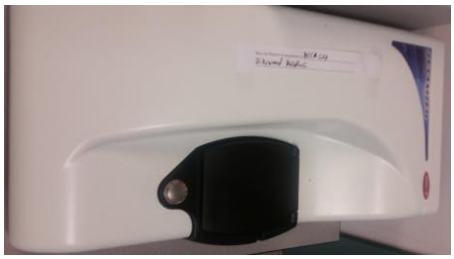

Figure 5.4: Malvern Zetasizer Nano-Z

Zeta potential is the electrical potential that occurs in the interfacial double plane, which is located at the slipping plane where there is an interface between a stationary layer of solvent attached to the particle and the dispersion medium (Hunter, 2013). The zeta potential was measured using a Malvern Zetasizer Nano-Z (figure 5.4). The zeta

potential is measured by placing the sample in an electric field and measuring how fast, and which direction the NCs move between the anode and cathode while suspended in a liquid solvent. Using this measurement, along with the viscosity of the solvent, the Zetasizer is able to calculate the zeta potential, which is an indicator of the NCs electrostatic stability in the liquid. The colloidal suspension is considered to be electrostatically stable if the zeta potential is greater than 20 mV or less than -20 mV. Bare nanocrystals, as well as crystals coated with oleic acid were examined this way.

5.2 Transmission Electron Microscopy of Lanthanide Fluorides

5.2.1. TEM Characterization of Cerium-Doped Dysprosium and Holmium Fluoride NCs

The first synthesis that we attempted was cerium doping of the dysprosium fluoride and holmium fluoride NCs. Cerium was chosen because of prior experiments that looked at cerium doping in lanthanum fluoride NCs (Withers et al., 2011), and to show that we could achieve similar implantation of cerium into dysprosium fluoride and holmium fluoride NCs.

HRTEM (figure 5.7 and 5.10) show fringing that is consistent with a orthophombic crystalline phase and is confirmed using FFT analysis (figures 5.5 and 5.8) (Williams and Carter, 1996). Figures 5.6 and 5.9 show wide areas to give an idea of how the NCs lay down in the grid, these images show a tight size distribution, of what appear to elongated hexagonal platelets laid out on the grid.

Figure 5.11 shows DyF_3:Ce10% nanocrystals. The fringes in this image have been measured and are consistent with the crystalline plane spacing of 0.253 nm which lines up with the expected 121 crystalline plane, 0.281 nm and 0.274 nm which match up with

the 210 crystalline plane, and 0.309nm which matches the 111 crystalline plane of holmium fluoride nanocrystals according to the ICDD databases (Brunton, et al., 1965). Figure 5.12 shows a very high resolution TEM image showing the crystalline plane spacing of a single DyF_3:Ce10%. Figure 5.13 is a wide field TEM image of DyF_3:Ce10% once again showing that we do have crystalline structure in our NCs after synthesis.

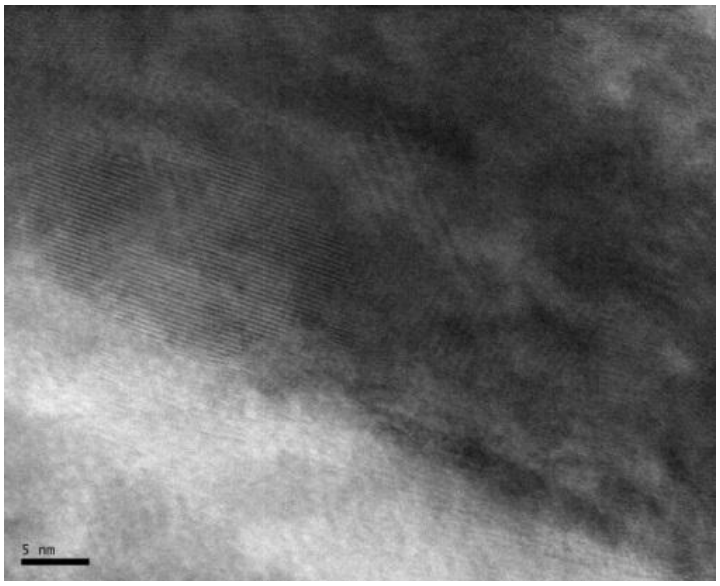

Figure 5.5: HRTEM of HoF_3:10%Ce, showing fringing from the crystalline planes. Reference bar is 5 nm.

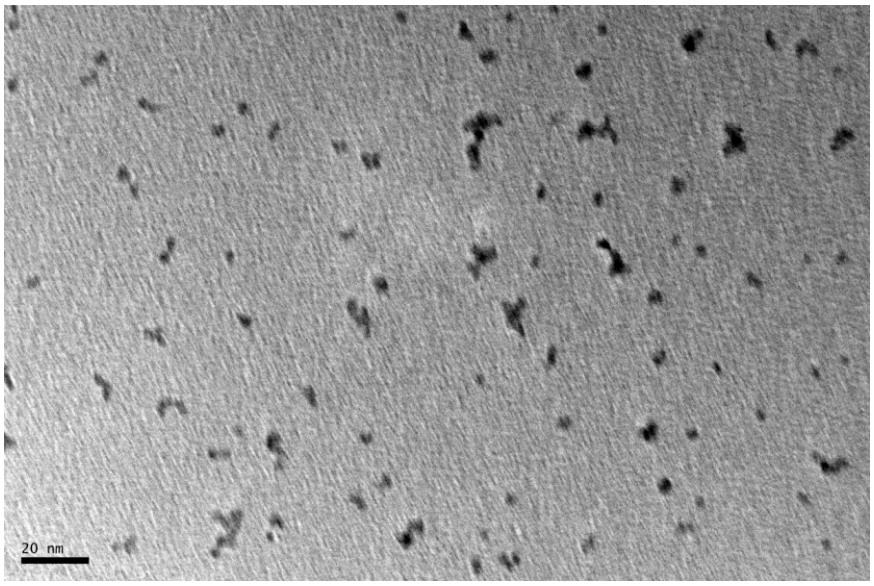

Figure 5.6: TEM of DyF_3:10%Ce, wide field image showing a tight size distribution.

Reference bar is 20 nm.

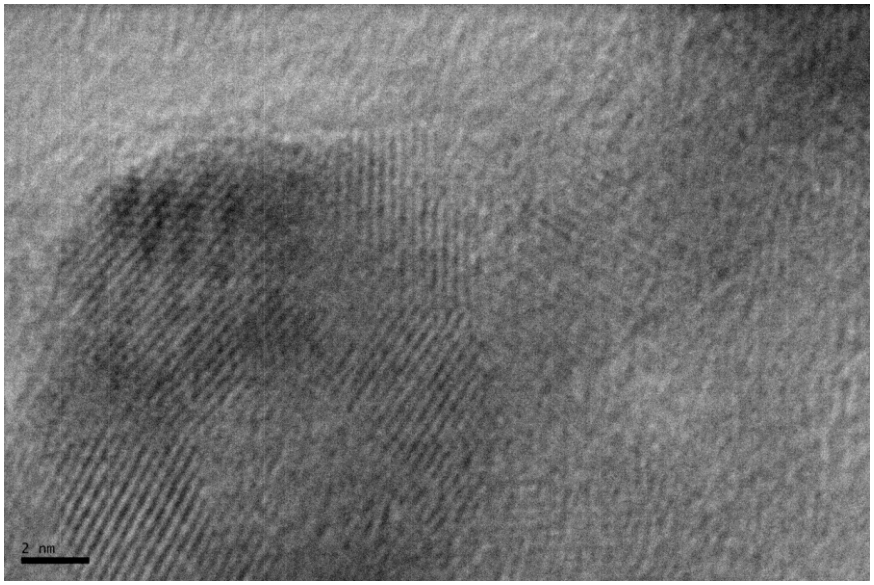

Figure 5.7: HRTEM of DyF_3:10%Ce showing fringes from the crystalline planes.

Reference bar is 2 nm.

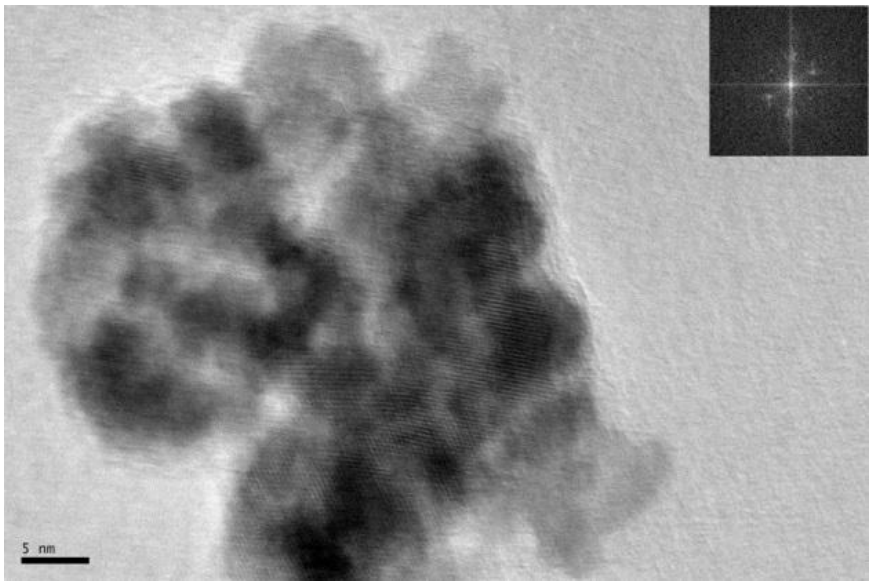

Figure 5.8: HRTEM of HoF_3:10%Ce with FFT analysis, showing fringing from the crystalline planes and FFT giving information about the phase of the crystals. Reference bar is 5 nm.

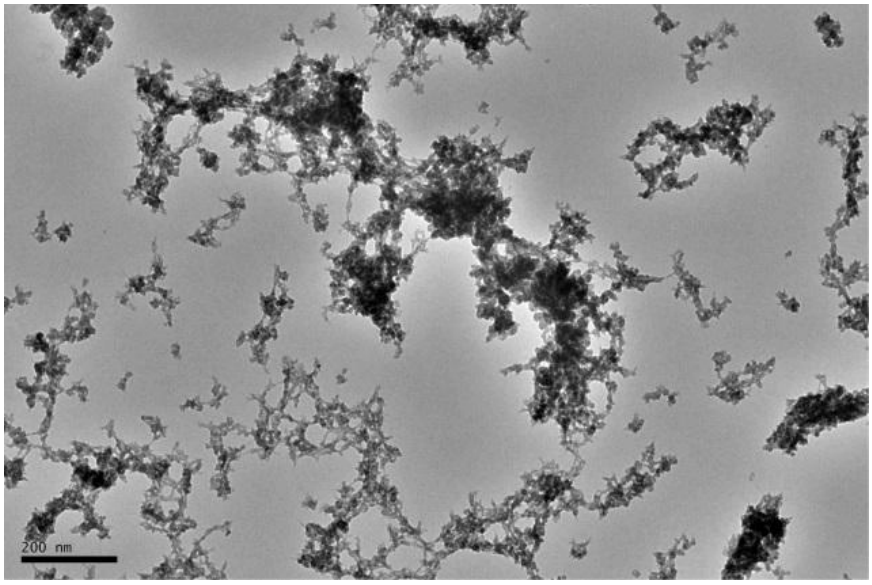

Figure 5.9: TEM of HoF_3:10%Ce, wide field image showing a tight size distribution. Reference bar is 200 nm.

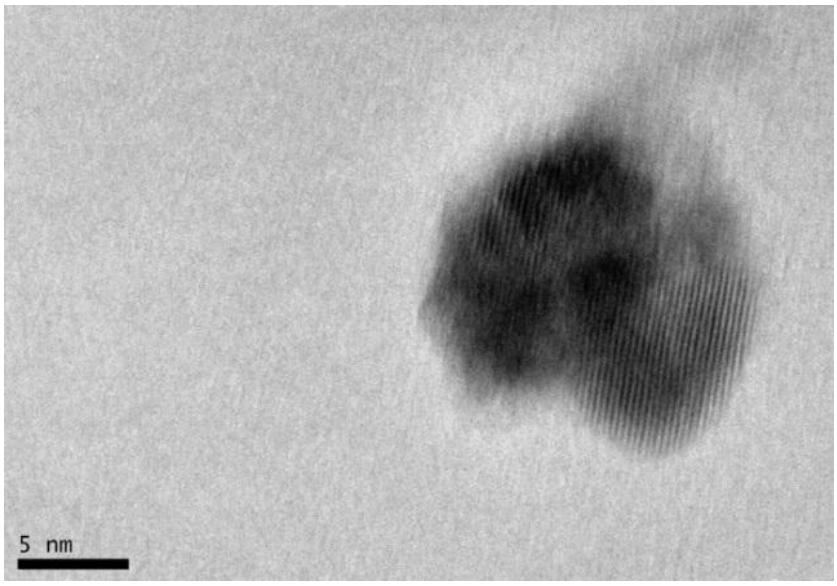

Figure 5.10: HRTEM of DyF_3:10%Ce showing fringes from the crystalline planes. Reference bar is 5 nm.

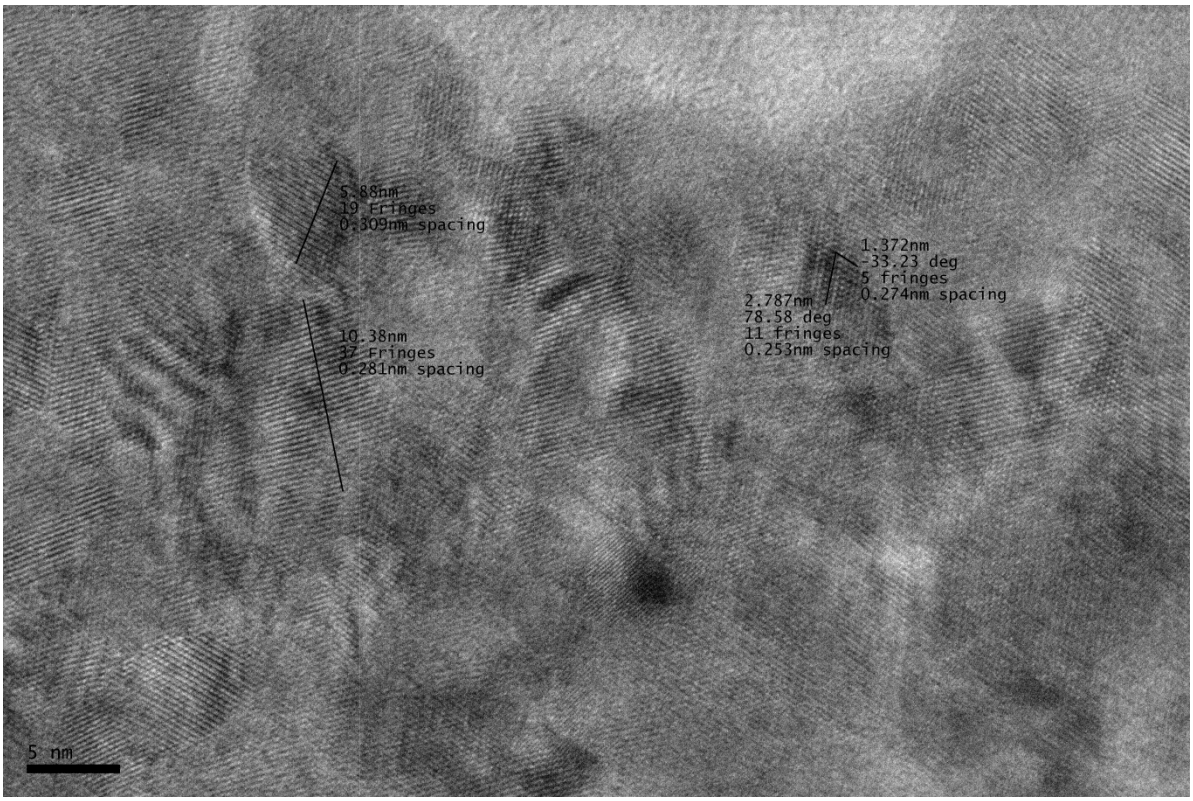

Figure 5.11: HRTEM of HoF_3:10%Ce with fringes from the crystalline planes measured using Digital Micrograph software. Reference bar is 5 nm.

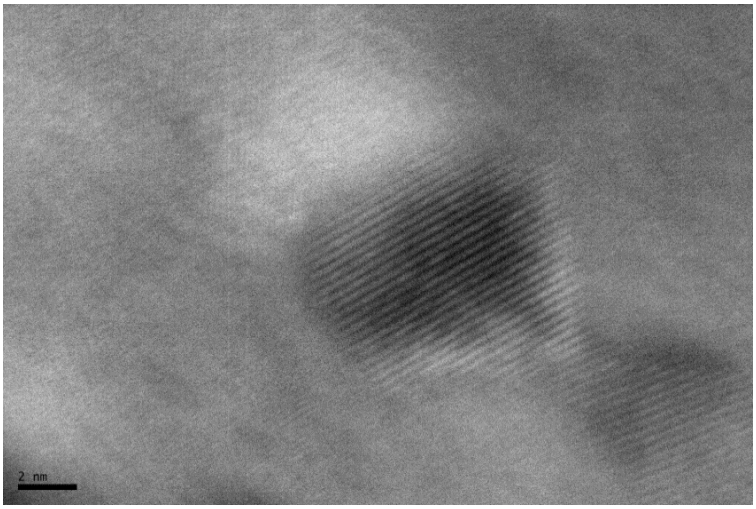

Figure 5.12: HRTEM of DyF_3:10%Ce showing fringes of a single crystal. Image shows no defects in the crystalline phase. Reference bar is 2 nm.

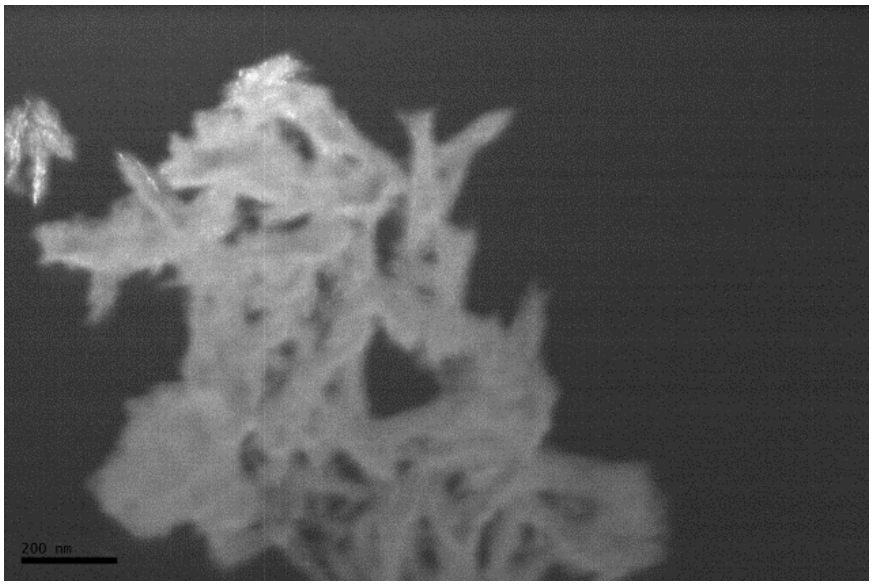

Figure 5.13: Dark field TEM of DyF_3:10%Ce, image of electrons diffracted by the crystal planes in the NCs. Shows that a periodic crystalline phase has been achieved. Reference bar is 200 nm.

5.2.2. TEM Characterization of Ytterbium-Doped Dysprosium and Holmium Fluorides

Next, nanocrystals were doped with ytterbium because of ytterbium's ability to enhance the emission from holmium (Quici et al., 2005). These NCs were synthesized using the same method as the cerium doped NCs, only replacing cerium with ytterbium, and showed similar results during structural analysis.

Figure 5.14 shows fringing from 2 NCs stacked on top of one another and suggests an octagonal shape similar to that of the un-doped samples above. The fringing in both figures 5.14 dysprosium, and 5.16 holmium, which are similar to that in the cerium doped samples above, once again suggest an orthorhombic crystalline lattice. Figures 5.15 and 5.17 both show a wide view of the NCs. They also reveal the way that the NCs tend to agglomerate when they are laid down onto the TEM grid. Figure 5.18 is a

dark field image which shows once again that the crystals produced from this synthesis are crystalline.

Figure 5.14: HRTEM of DyF_3:10%Yb showing fringes from the crystalline planes. Reference bar is 5 nm.

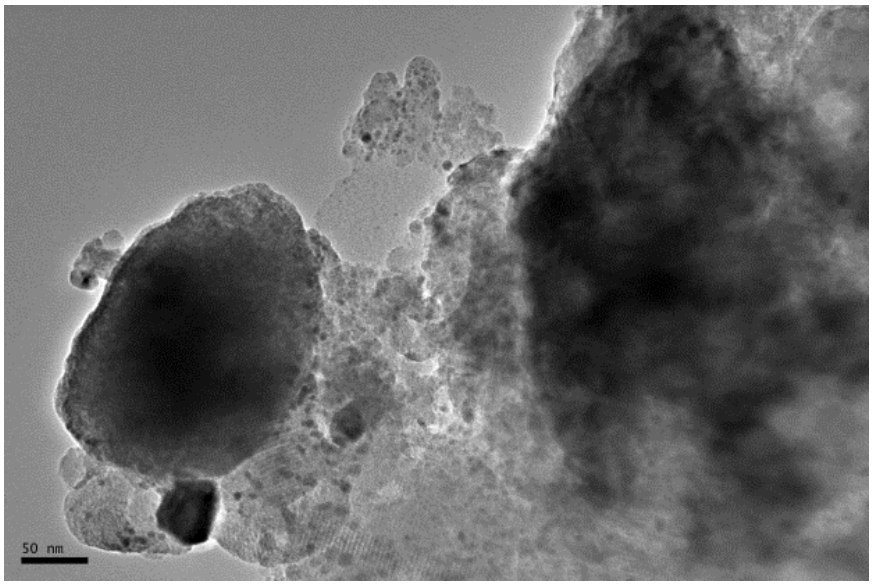

Figure 5.15: TEM of DyF_3:10%Yb, wide field image showing NCs inside of un-evaporated toluene and oleic acid. Reference bar is 50 nm.

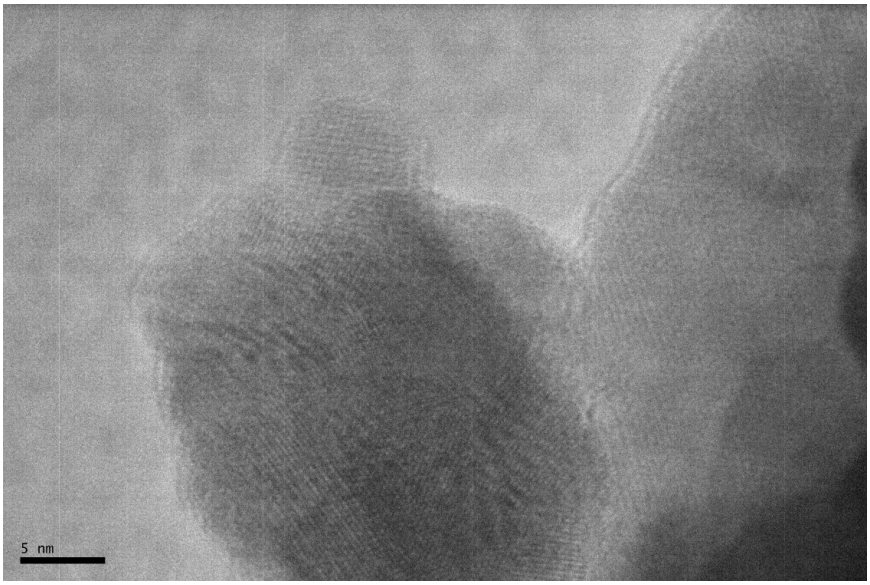

Figure 5.16: HRTEM ofHoF_3:10%Yb showing fringes from the crystalline planes. Reference bar is 5 nm.

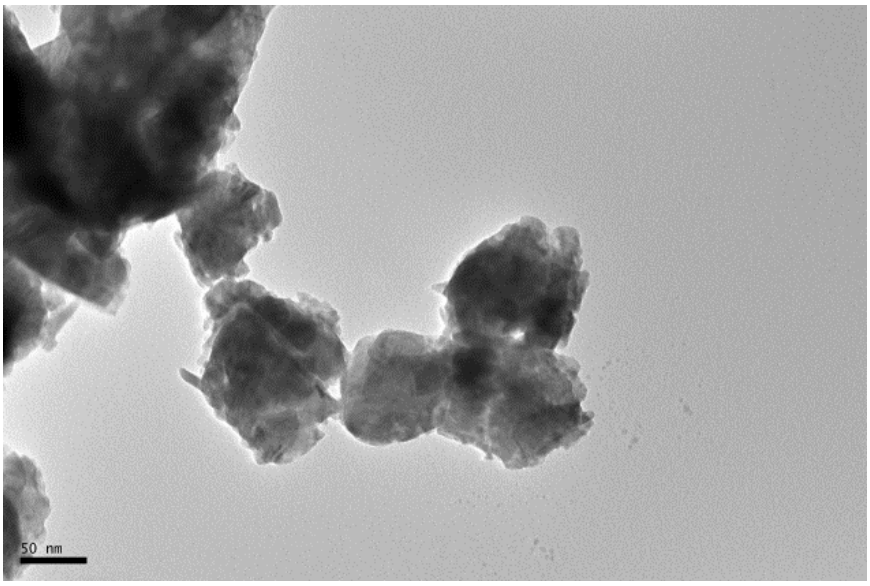

Figure 5.17: TEM of HoF_3:10%Yb, showing agglomerations of NCs on the grid. Reference bar is 50 nm.

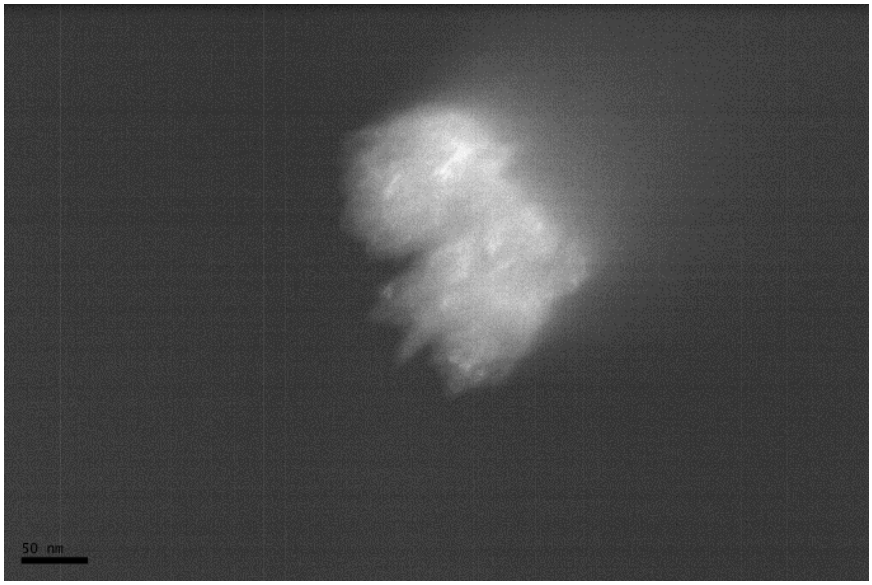

Figure 5.18: Dark field TEM of HoF_3:10%Yb, image of electrons diffracted by the crystal planes in the NCs. Shows that a periodic crystalline phase has been achieved. Reference bar is 50 nm.

5.3 Energy Dispersive X-Ray Spectroscopy (EDS) of Lanthanide Fluorides

Figures 5.19 shows EDS spectra from dysprosium fluoride doped with cerium. The image shows the presence of dysprosium, cerium and fluoride as expected in the NCs, as well as carbon, copper and oxygen. The carbon and copper are from the TEM grid, which is a copper coated carbon grid, and the oxygen is bonded to the surfaces in the chamber including the outer layers of the NCs.

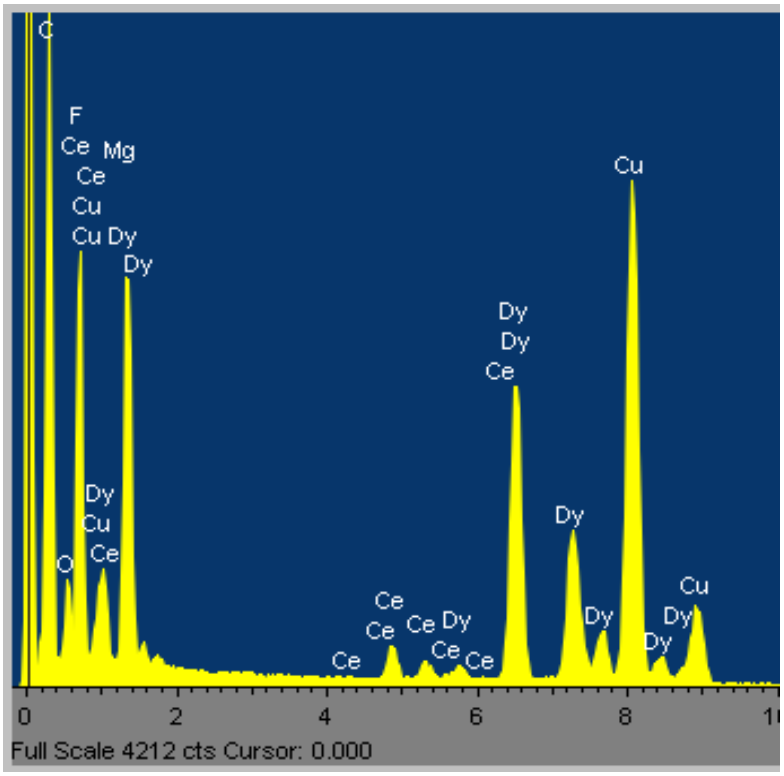

Figure 5.19: EDS of DyF_3:10%Ce, X-ray spectra showing the atomic constituents by X-ray energy from e^- k-shell interactions.

Figure 5.20 shows EDS spectra from holmium fluorine doped with cerium. The image once again shows the presence of holmium, cerium and fluoride as expected in the NCs. Like before it also shows carbon and copper from the TEM grids and oxygen from

the surfaces. Here we also see a signal for iron, which is from the chamber, and a signal identified as promethium that shares peaks with holmium and cerium, the promethium can be discounted as a misidentification both because it shares peaks and, importantly, because it is a man-made element with a very short half-life and thus extremely unlikely here.

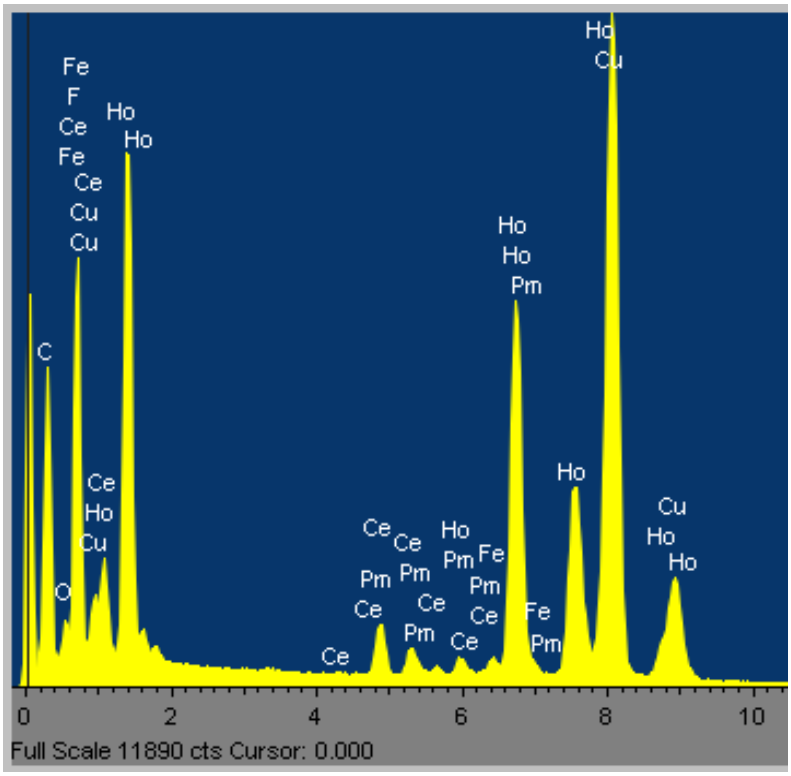

Figure 5.20: EDS of HoF_3:10%Ce, X-ray spectra showing the atomic constituents by X-ray energy from e^- K-shell interactions.

5.4 X-ray Diffraction (XRD) of Lanthanide Fluorides

The XRD spectra was analyzed using the COD (Downs and Hall-Wallace, 2003; Gražulis et al., 2009; Gražulis et al., 2012) and the ICDD databases (Brunton, et al., 1965; Faber and Fawcett, 2002; Fawcett et al., 2009) to determine the crystalline

structure of the NCs. Figure 5.21 shows the XRD data for HoF_3:10%Yb, matched to the data for orthorhombic HoF_3 ICDD card number 00-023-0284 (Faber and Fawcett, 2002; Fawcett et al., 2009). The slight mismatch in the lattice is from the strain caused by the insertion of ytterbium into the lattice. This orthorhombic lattice assembles into the elongated hexagonal platelets that are visible in the TEM images.

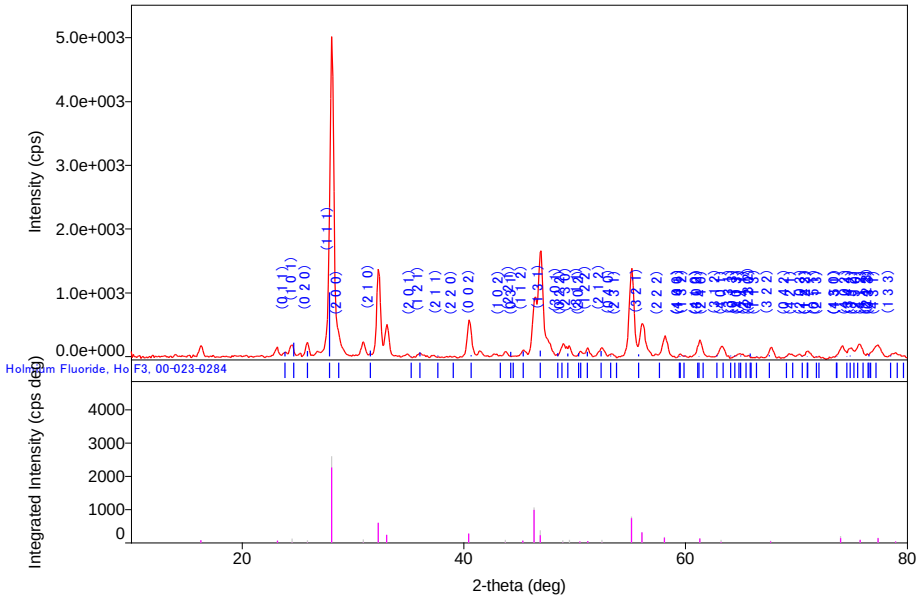

Figure 5.21: XRD of HoF_3:10%Yb, matched to the ICDD database card for HoF_3. The strain from the inclusion of ytterbium in the lattice is seen as a slight shift in the peak positions.

5.5 Dynamic Light Scattering (DLS) and Zeta-Potential of Lanthanide Fluorides

Figures 5.22 thru 5.25 give dynamic light scattering (DLS) data. This measurement gives the hydrodynamic size of the particles being studied.

In figure 5.22 oleic acid (OA) coated DyF_3:10%Yb nanocrystals were measured and shown to have a mean diameter of approximately 13.21 nm +/- 1.58 nm. This

measurement shows a tight size distribution for this synthesis, which is confirmed in the other measurements. Similarly figures 5.23 and 5.24 showing DLS data for undoped DyF_3 and HoF_3:10%Yb mean diameters of 13.52 nm +/- 2.59 nm and 14.77 nm +/- 3.19 nm were measured. These distributions show a small variation in size of the nanocrystals produced. To show the size difference between the coated and uncoated NCs figure 5.27 shows the size distribution for a sample of DyF_3:10%Yb:10%Ho, for which no OA coating is present, and shows a mean diameter of 5.98 nm +/- 1.92 nm. These measurements along with data from TEM and EDS show that high quality crystals with a small size distribution have been obtained from our synthesis method.

The use of DLS also allows for the interrogation of a much larger sample of the crystals present in solution, then that of TEM imaging, and, therefore results in a better statistical analysis of the size distribution of the sample. Looking at the HRTEM images in section 5.2.1 and 5.2.2 an agreement between the size distribution seen in DLS and the size of individual crystals imaged in the TEM can be made. Using these two methods to complement each other gives a size of approximately 6 nm and a coating thickness of approximately 3.75 nm when coated with oleic acid.

Additionally zeta potential was measured. The samples that were coated with oleic acid consistently averaged a zeta potential of 73 mV +/- 2 mV, this measurement is due to the oleic acid interacting with the toluene. The oleic acid is also compatible with the PMMA, which is why we choose this surfactant in the first place. This measurement shows that they are very stable in the toluene solution. Toluene is one of the precursors for PMMA and therefore the oleic acid coating allowed for a uniform distribution when the PMMA was polymerized. The powder samples were also put into toluene and

measured, as a contrast to the coated NCs. The uncoated samples all measure between -1 mV and 0 mV. This shows that as expected the uncoated samples are not stable in the toluene solution, and quickly flocculate out.

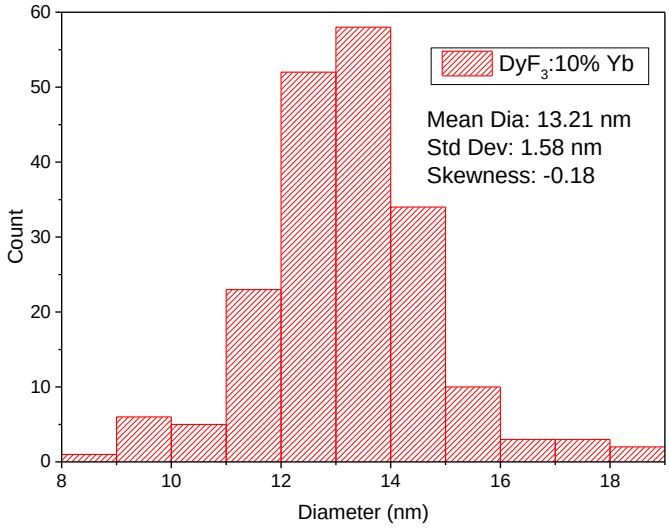

Figure 5.22: DLS of OA-coated DyF_3:10%Yb, showing a tight size distribution of particle size, similar across samples.

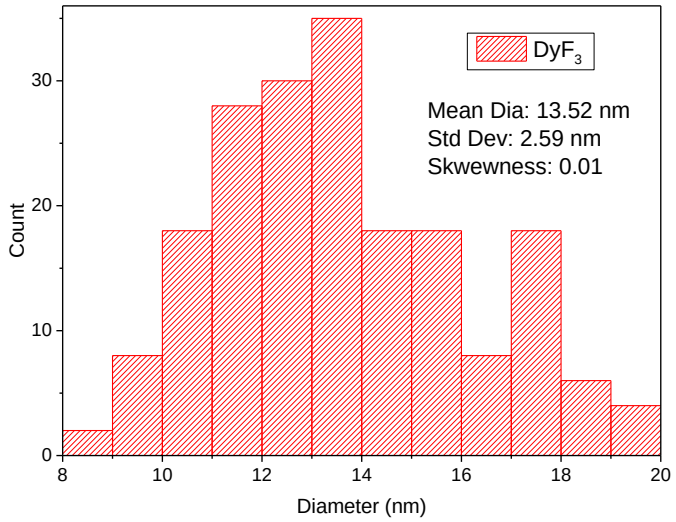

Figure 5.23: DLS of OA-coated DyF_3, showing a tight size distribution of particle size, similar across samples.

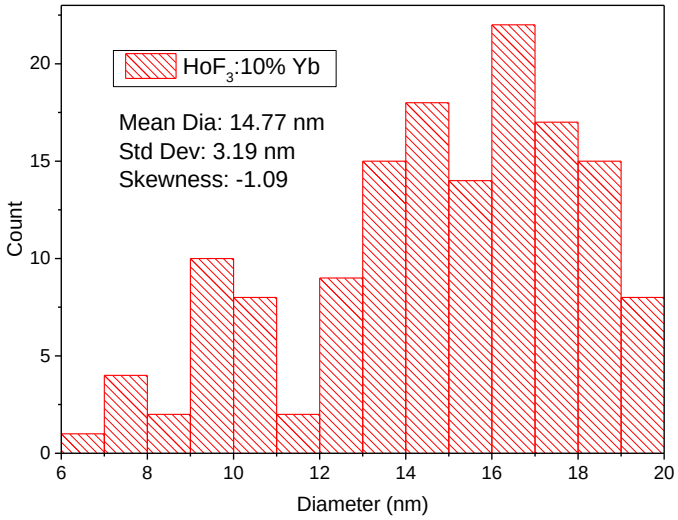

Figure 5.24: DLS of OA-coated HoF_3:10%Yb, showing a tight size distribution of particle size, similar across samples.

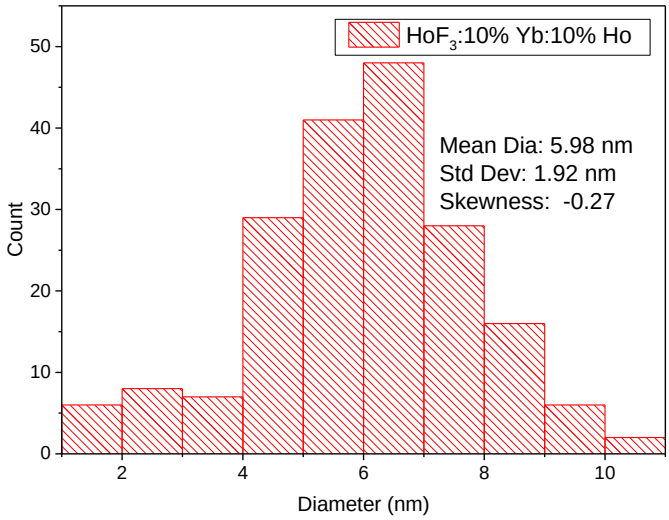

Figure 5.25: DLS of uncoated DyF_3:10%Yb:10%Ho, showing a tight size distribution of particle size, similar across samples. The uncoated sample shows a smaller mean diameter giving insight into the thickness of the oleic acid coating.

5.6. Conclusion

The characterization shows that it is possible, using our synthesis, to produce high quality lanthanide fluoride NCs, with a tight size distribution, and few defects in the crystalline lattice. These NCs can be coated with different surfactants to allow them to be incorporated into polymers, and they can be synthesized as powders with no surfactants so that they can be used as powders or incorporated into other crystalline matrices.

Chapter 6

Neutron Flux Experiments

6.1. UV/Vis Absorption Equipment

We measured spectral absorption from the samples using a Cary 5000 spectrometer (figure 6.1). The Cary 5000 has a dual sample holder so that the measurement can subtract out the absorption of the any solvent or polymer host that may be used to suspend the NCs during measurement and allows for a quicker measurement as background is subtracted during data collection.

Figure 6.1: Cary 5000 spectrophotometer

6.2. Neutron Flux Experiment with PMMA loaded with Oleic-Acid-Coated DyF_3

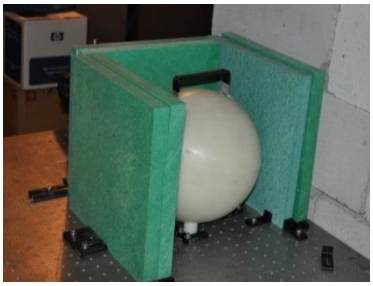

Figure 6.2: Polyethylene sphere surrounded by borated boards

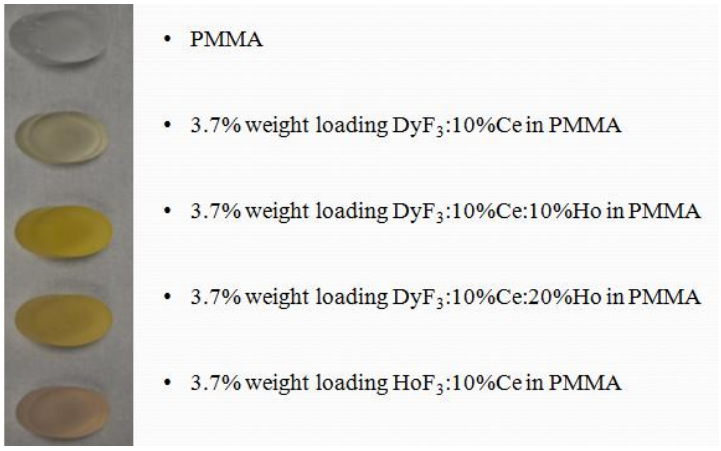

Figure 6.3: Image of PMMA loaded with dysprosium fluoride NCs with varying amounts of Ho content, shows visible differences between samples with and without holmium in the crystalline matrix.

Figures 6.4 shows comparisons of NCs suspended in PMMA (figure 6.3). The crystals were not only synthesized with different amounts of holmium present, pure DyF_3 was exposed to neutron radiation using the setup shown in figure 6.2. The nanocrystals were irradiated using a ^{252}Cf source with a calculated activity of 5.3×10^6 n/s. The polyethylene sphere, with a radius of 12.7 cm, was used to moderate the neutrons giving a flux of thermal neutrons thru the sample, resulting in a flux through the sample of 2.6×10^3 n/cm^{2}s. The green borated boards in figure 6.2 are there as a layer of protection for anyone working with the experiment. The samples were then attached to the surface of the sphere and left there for 3.9×10^5 s. This configuration resulted in a total fluence of 1.023×10^9 n/cm^2. Absorbance measurements were taken using the setup described in section 6.1.

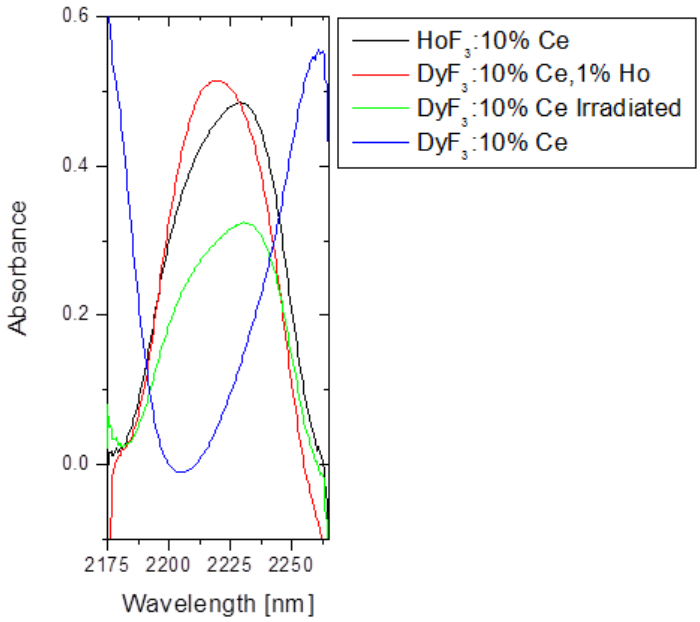

Figure 6.4: Comparison of NCs capped with oleic acid and suspended in PMMA, shows a qualitative difference between samples containing holmium and those not containing holmium.

Figure 6.4 shows that there is a difference in the absorption from HoF_3 to DyF_3 in the OA coated samples dispersed in toluene, and then polymerized in a PMMA matrix. This difference is enough to qualify that Ho is present in the fluoride, but does not provide the ability to quantify the amount of Ho present.

6.3. Neutron Flux Experiment with KBr loaded with Annealed DyF_3 Powder

Figure 6.6 shows comparisons of NCs pressed into KBr discs (figure 6.5). The crystals were not only synthesized with different amounts of holmium present, pure DyF_3 was exposed to neutron radiation using the setup shown in figure 6.2. The nanocrystals were irradiated using a ^{252}Cf source with a calculated activity of 4.3 x 10^6 n/s. The

polyethylene sphere, with a radius of 12.7 cm, was again used to moderate the neutrons giving a flux of thermal neutrons thru the sample, resulting in a flux through the sample of 2.1 x 10^3 n/cm^{2}s. The green borated boards in figure 6.2 capture neutrons and are there as a layer of protection for anyone working with the experiment. The samples were then attached to the surface of the sphere and left there for 3.9 x 10^6 s. This configuration resulted in a total fluence of 8.3 x 10^8 n/cm^2. Absorbance measurements were taken using the setup described in section 6.1.

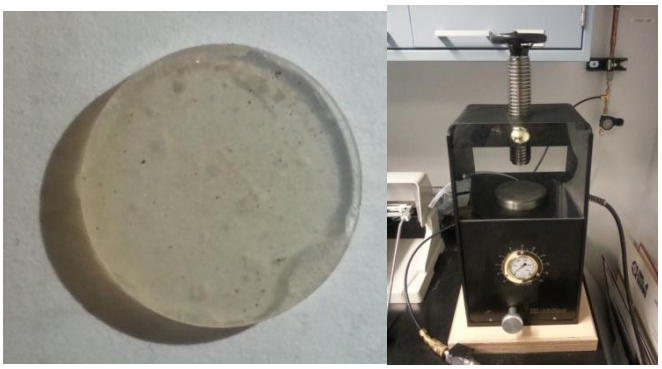

Figure 6.5: Image of KBR loaded with dysprosium fluoride NCs and the press used to create the KBr disc.

Figure 6.6 shows the measurement of the powder samples. Although there are differences in the absorbance, there is once again no way of using this method to determine with enough precision the holmium content of the samples.

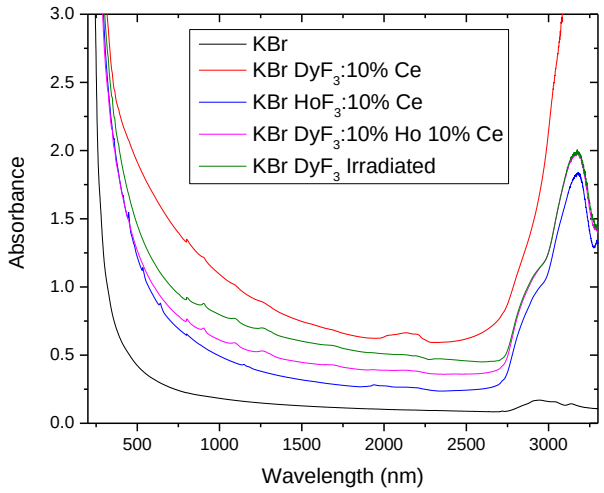

Figure 6.6: Comparison of absorbance of NCs in KBr matrix shows the overall absorption of the samples, with differences hard to detect at this wavelength resolution.

6.4. Conclusion

Using absorption measurements, a qualitative analysis can be made on whether or not there is holmium present in the crystals, and photoluminescence can also be used to determine the presence of holmium in the samples. There is no absorbance data for the powder samples made later in this study because there was no dry sample holder for the setup, and the NCs flocculate out of the toluene solution before the measurement is able to complete, these samples were measured using PL which is discussed in chapter 7.

Chapter 7

Photoluminescence of Holmium Fluoride

7.1. Photoluminescence (PL)

For a short time we were able to build a system using a Continuum laser at CINT which was used to obtain PL in the 2.1 μm range, and to see the up conversion emission from holmium in the samples doped with ytterbium. The setup used a Continuum LASER as a tunable source, and implementing diffraction gratings to focus a specific wavelength of light on the sample and then routes the emission from the sample onto a detector to record the emission intensity. The setup at CINT used IR transparent fiber optics to direct the light from the excitation source to the sample, and finally to route the emission from the sample to the detector.

7.2. Photoluminescence (PL) of Lanthanide Fluorides

When excited at 980 nm holmium has two emission lines at 2.1 μm and 2.4 μm, this emission is enhanced with ytterbium doping (Kurkov et al., 2009; Luo and Cao, 2007). Ytterbium doping also enhances the up-conversion (when two photons are absorbed and a single photon is emitted with a higher energy then the individual excitation photons) emission seen in figure 7.1 when excited at 980nm (Luo and Cao, 2007). Measurements of the 2.1 μm (figure 7.2) emission were taken using the setup described in section 7.1 above. The 2.4 μm emission was not observed because of limitations of the infrared detector which could only detect up to 2.3 μm.

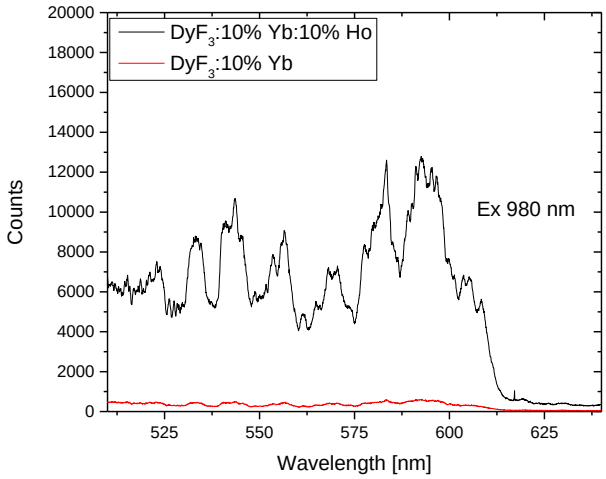

Figure 7.1: Up conversion spectrum from DyF_3:10%Yb:10%Ho compared to that of DyF_3:10%Yb under 980 nm excitation, shows that the up conversion due to holmium does not show up in dysprosium samples.

Figure 7.1 shows the up-conversion emission of DyF_3:10%Yb:10%Ho NCs compared to DyF_3:10%Yb NCs. The data clearly shows a difference in emission of NCs containing holmium and those which do not.

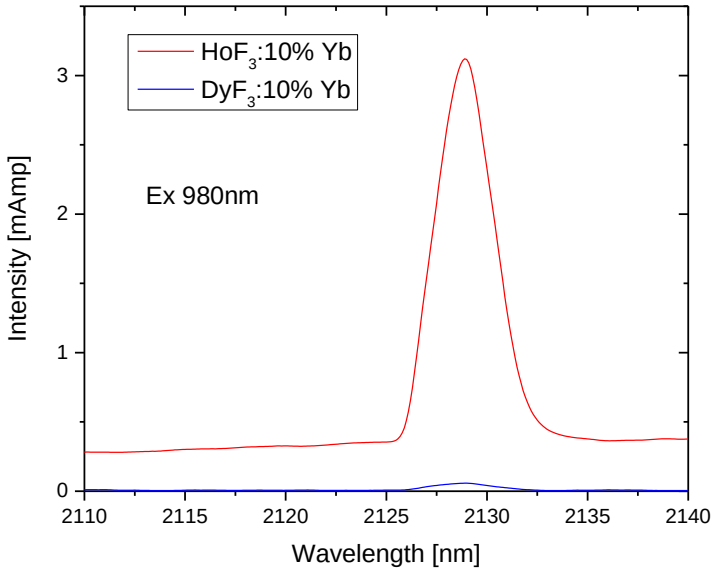

Figure 7.2: SWIR emission of HoF_3:10%Yb compared to DyF_3:10%Yb under 980 nm excitation, give a clear indication that the 2.13 µm emission from holmium allows it to be distinguished from dysprosium samples as there is no emission from the dysprosium at this wavelength.

Figure 7.2 shows the short-wavelength infrared (SWIR) emission from HoF_2:10%Yb NCs compared to DyF_3:10%Yb NCs. The data shows a strong emission from the holmium sample at 2.13 µm while the dysprosium shows no emission within this wavelength region. This peak along with the expected peak at 2.4 µm could be used, given adequate quantum efficiency, to compare the holmium content in the matrix from a sample before and after irradiation.

7.3 Conclusion

We were able to see emission from holmium in the powder samples. These measurements included both 2.13 μm emission as well as the up conversion emission from the samples. Further measurement of the photoluminescence for comparison of dysprosium samples with varying doping levels would be useful but were not performed due to access limitations with the equipment.

Chapter 8

Conclusions and Further Directions of Research

This chapter presents the conclusions draw from the research presented here. This includes an explanation of future work and challenges that still need to be taken on to design a working device.

8.1. Conclusions:

First the current state of neutron detectors being used today was discussed, and although they are all very good methods for their own type of detection, none of them offer all of the aspects that a clandestine and forensic dysprosium detector could offer. Next the neutron interactions with dysprosium are discussed. Here we show that dysprosium-164 has a 28.2% natural abundance in dysprosium samples and does not need to be purified to be a detector candidate. It is also shown that all other isotopes of dysprosium can feed into dysprosium-164 upon neutron captures. This leads to the fact that if we could non-destructively obtain highly accurate isotropic information before and after exposure, one could then possibly determine many aspects of the event. This of course is not possible with current technology. Finally this dissertation looked at other neutron captors, and here it is shown that dysprosium has many advantages in this application, including a high thermal neutron cross-section, after neutron capture and β^- decay a stable holmium atom is produced, and the similar chemical properties of holmium and dysprosium leads to a stable crystal lattice.

First we developed a mathematical model to determine the minimum detectability of a dysprosium fluoride forensic detector, and to look at the production both holmium and erbium from neutron capture in a dysprosium fluoride matrix. The model was based on a 100% dysprosium fluoride matrix. Using information obtained from Hamamatsu as well as universal constants we were able to show that, assuming a 1 m path length, through a 2.5 cm diameter detector, focused onto a 1 cm spot, the detector can detect a holmium loading of 9.6×10^{18} Ho atoms/cm^3. The Bateman equations were then used to determine the products produced during and after the samples were introduced into a neutron flux. A 7 day irradiation and a 3 day rest period, resulting in a 10 day period of production, was assumed. This time table was decided on based on the average time a container takes to cross the Atlantic Ocean from Europe to the United States. Using these data points, the model says that with a flux of 1×10^6 n/cm^{2}s, we can expect to see a concentration that exceeds the minimum detectability of 9.6×10^{18} Ho atoms/cm^3. We also show that although erbium would not be detectable at lower fluxes, after a neutron flux of 1×10^{10} n/cm^{2}s the erbium produced does begin to exceed the minimum detectability threshold of the system.

Next we presented the colloidal syntheses of lanthanide fluorides. The laboratory setup was explored along with a quick overview of the lab equipment used. The synthesis was used to produce, DyF_3, HoF_3, DyF_3:10%Yb, HoF_3:10%Yb, HoF_3:10%Ce, DyF_3:10%Ho DyF_3:10%Ce, DyF_3:10%Ce10%Ho and DyF_3:10%Yb10%Ho, using molar ratios to determine the doping of the lanthanides in the nanocrystals. Other lanthanide fluorides have also been synthesized in the lab described, and include lanthanum, praseodymium, gadolinium, and erbium fluorides, as well as dopants at varying levels

such as cerium, europium and ytterbium. The dopants are used to enhance the inherent optical properties of the constituent nanoparticles.

The synthesis was used to obtain two different conformations of the nanocrystals, which were used in this dissertation. These variations allow for customization of the nanocrystals depending on their final configuration. The synthesis is based on a hydroxyl method. This method allows for the nanocrystals to be dried into a powder and then annealed obtaining a highly luminescent powder or for an oleic acid surfactant to be attached to the nanocrystal surface. Dried powders were used for the IR photoluminescence study because a powder was needed to take advantage of the PL setup built at CINT, and also for nanocrystals which were annealed and loaded into a KBr disc. The oleic acid synthesis was used for nanocrystals that would be suspended in toluene and then polymerized into PMMA, allowing for an even distribution of nanocrystals inside of the polymer.

Next we looked at the structural characterization of the nanocrystals and shows that the work has been able to produce high quality crystalline nanocrystals. The combination of methods including TEM, EDS, XRD, DLS and zeta potential allow us to see that all of the expected components are present on the nanocrystals made in the lab and that they are high quality, defect free nanocrystals.

Next neutron flux experiments were performed on samples of nanocrystals loaded into PMMA and KBr matrices. Absorption was used for these early experiments, because of a lack of access to a proper PL setup, these experiments showed that although we could see the difference between holmium containing nanocrystals and those nanocrystals

which did not contain holmium, as well as a difference in those that had been exposed to radiation. The experiments did not show enough of a difference to give a quantitative distinction, and therefore only a qualitative analysis is possible using these methods.

Next an experiment was done at CINT, and PL from the 2.1 μm line was able to be resolved from a powder sample of HoF_3 and compared to a DyF_3 sample. Up-conversion was also observed from a DyF_3:10%Ho:10%Yb powder sample and compared to a DyF_3:10%Yb powder sample. This data is promising, but the short time period that we were allowed to work with this setup, did not allow for further investigation of this avenue. The setup was also limited, because we were unable to look at the 2.4 μm line which would allow for a comparison and a more quantitative analysis of the materials.

The first experiments used PMMA and KBr. These mediums have since been replaced with powders for now and in the future may also be replaced with either silicon polymers or infrared fiber optics. PMMA was dropped because it has an absorption line around 2.1 μm due to the carbon bonds, and the KBr was discontinued because of the fragile nature of the crystals.

8.2. Further Directions of Research

Future work in this area needs to include methods that extend the path length of the optical interrogation, of the samples before and after neutron irradiation, to enhance detectability. These should include loading silicone polymers with dysprosium fluoride that could be put into a resonator to increase the path length of the sample, so that the photons can pass through multiple times extending the path length they see in the

material. This can be setup in a CW format as shown in the basic setup in figure 3.2. To build this setup there will be a need for access to a high intensity 980 nm source as well as a very sensitive detector that can detect both 2.1 μm and 2.4 μm, such as the Hamamatsu InSb detector used to determine the minimum detectability in chapter 3. Work also needs to be done to look at the radiation hardness of the NCs, to see if defects in the crystalline lattice can be detected using TEM after high flux exposure of the NCs. This experiment would require access to a very high flux of both neutrons and gamma irradiation to determine how stable the crystals are under these conditions. If defects are found, the NCs could be annealed again at 1200 °C to see if the crystalline lattice could be brought back to a defect free state.

References

Aime, S., A. Barge, D. Delli Castelli, F. Fedeli, A. Mortillaro, F. U. Nielsen, and E. Terreno, 2002, Paramagnetic lanthanide (III) complexes as pH-sensitive chemical exchange saturation transfer (CEST) contrast agents for MRI applications: Magnetic Resonance in Medicine, v. 47, p. 639-648.

Akiyama, S., H. Ishibashi, T. Utsu, C. L. Melcher, and J. S. Schweitzer, 1993, Cerium doped gadolinium silicate, output is good match with sensitivity of bi-alkali photomultiplier tube, United States patent 5,264,154, issued 23 November 1993.

Allain, J., M. Monerie, and H. Poignant, 1991, High-efficiency CW thulium-sensitised holmium-doped fluoride fibre laser operating at 2.04 μm: Electronics Letters, v. 27, p. 1513-1515.

Bateman, H., 1910, The solution of a system of differential equations occurring in the theory of radioactive transformations: Proc. Cambridge Philos. Soc, p. 423-427.

Bragg, W. H., and W. L. Bragg, 1913, The reflection of X-rays by crystals: Proceedings of the Royal Society of London. Series A, Containing Papers of a Mathematical and Physical Character, p. 428-438.

Brunton, G. D., Insley, H., McVay, T. N., & Thoma, R. E. (1965). *Crystallographic data for some metal fluorides, chlorides, and oxides* (No. ORNL-3761). Oak Ridge National Lab., Tenn..

Cetnar, J., 2006, General solution of Bateman equations for nuclear transmutations: Annals of Nuclear Energy, v. 33, p. 640-645.

Chatteriee, D. K., A. J. Rufalhah, and Y. Zhang, 2008, Upconversion fluorescence imaging of cells and small animals using lanthanide doped nanocrystals: Biomaterials, v. 29, p. 937-943.

Cutler, C. S., C. J. Smith, G. J. Ehrhardt, T. T. Tyler, S. S. Jurisson, and E. Deutsch, 2000, Current and potential therapeutic uses of lanthanide radioisotopes: Cancer biotherapy & radiopharmaceuticals, v. 15, p. 531-545.

Czirr, J., G. MacGillivray, R. MacGillivray, and P. Seddon, 1999, Performance and characteristics of a new scintillator: Nuclear Instruments and Methods in Physics Research Section A: Accelerators, Spectrometers, Detectors and Associated Equipment, v. 424, p. 15-19.

d'Errico, F., and A. J. Bos, 2004, Passive detectors for neutron personal dosimetry: state of the art: Radiation Protection Dosimetry, v. 110, p. 195-200.

Davidson, N., and B. Koppelman, 2008, Detecting Nuclear and Radiological Materials, RS policy document, http://www.nuclearfiles.org/menu/key-issues/nuclear-weapons/issues/governance/international-coop/PDFs/displaypagedoc%5B1%5D.pdf, The Royal Society.

Downs, R. T., and M. Hall-Wallace, 2003, The American Mineralogist crystal structure database: American Mineralogist, v. 88, p. 247-250.

Dunning, J., G. Pegram, G. Fink, and D. Mitchell, 1935, Interaction of neutrons with matter: Physical Review, v. 48, p. 265.

Ely, J. H., L. E. Erikson, R. T. Kouzes, A. T. Lintereur, and D. C. Stromswold, 2009, Lithium loaded glass fiber neutron detector tests, Pacific Northwest National Laboratory.

Faber, J., and T. Fawcett, 2002, The powder diffraction file: present and future: Acta Crystallographica Section B: Structural Science, v. 58, p. 325-332.

Fawcett, T., F. Needham, C. Crowder, and S. Kabekkodu, 2009, Advanced materials analysis using the powder diffraction file: Proceedings of the 10th National Conference on X-ray Diffraction and ICDD Workshop, Shanghai, China, October, p. 1-3.

Firestone, R. B., 2000, The Berkeley Laboratory Isotopes Project, Exploring the Table of Isotopes: May, v. 22, p. 1.

Furetta, C., J. Tuyn, F. Louis, J. Azorin, and C. Driscoll, 1986, Simultaneous determination of dose and elapsed time in accident dosimetry using thermoluminescent materials: Radiation Protection Dosimetry, v. 17, p. 161-164.

Gražulis, S., D. Chateigner, R. T. Downs, A. Yokochi, M. Quirós, L. Lutterotti, E. Manakova, J. Butkus, P. Moeck, and A. Le Bail, 2009, Crystallography Open Database–an open-access collection of crystal structures: Journal of Applied Crystallography, v. 42, p. 726-729.

Gražulis, S., A. Daškevič, A. Merkys, D. Chateigner, L. Lutterotti, M. Quirós, N. R. Serebryanaya, P. Moeck, R. T. Downs, and A. Le Bail, 2012, Crystallography Open Database (COD): an open-access collection of crystal structures and platform for world-wide collaboration: Nucleic Acids Research, v. 40, p. D420-D427.

Haskin, L. A., and F. A. Frey, 1966, Dispersed and not-so-rare earths: Science, v. 152, p. 299-314.

Hawkesworth, M., and J. Walker, 1969, Review: Radiography with neutrons: Journal of Materials Science, v. 4, p. 817-835.

Hunter, R. J., 2013, Zeta potential in colloid science: principles and applications, v. 2, Academic Press.

Kurkov, A., E. Sholokhov, O. Medvedkov, V. Dvoyrin, Y. N. Pyrkov, V. Tsvetkov, A. Marakulin, and L. Minashina, 2009, Holmium fiber laser based on the heavily doped active fiber: Laser Physics Letters, v. 6, p. 661-664.

Lintereur, A. T., R. T. Kouzes, J. H. Ely, L. E. Erikson, E. R. Siciliano, and M. L. Woodring, 2009, Boron-lined neutron detector measurements, Pacific Northwest National Laboratory.

Liu, F., J. Y. Park, Y. Zhang, C. Conwell, Y. Liu, S. R. Bathula, and L. Huang, 2010, Targeted cancer therapy with novel high drug-loading nanocrystals: Journal of Pharmaceutical Sciences, v. 99, p. 3542-3551.

Liu, Z., and R. Peng, 2010, Inorganic nanomaterials for tumor angiogenesis imaging: European Journal of Nuclear Medicine and Molecular Imaging, v. 37, p. 147-163.

Luo, X.X., and W.H. Cao, 2007, Upconversion luminescence of holmium and ytterbium co-doped yttrium oxysulfide phosphor: Materials Letters, v. 61, p. 3696-3700.

McGregor, D., T. Unruh, and W. McNeil, 2008, Thermal neutron detection with pyrolytic boron nitride: Nuclear Instruments and Methods in Physics Research Section A: Accelerators, Spectrometers, Detectors and Associated Equipment, v. 591, p. 530-533.

McLaren, A. B., E. L. R. Hetherington, D. J. Maddalena, and G. M. Snowdow, 1988, *The Development of Dysprosium-165 Hydroxide Macroaggregates for Radiation*

Synovectomy, Australian Nuclear Science and Technology Organization, Lucas Heights Research Laboratories,.

McNaught, A. D., 1997, Compendium of Chemical Terminology, v. 1669, Blackwell Science Oxford.

Menge, P. R., G. Gautier, A. Iltis, C. Rozsa, and V. Solovyev, 2007, Performance of large lanthanum bromide scintillators: Nuclear Instruments and Methods in Physics Research Section A: Accelerators, Spectrometers, Detectors and Associated Equipment, v. 579, p. 6-10.

Merbach, A. E., and É. Tóth, 2001, The chemistry of contrast agents in medical magnetic resonance imaging, v. 46, Wiley Online Library.

Naccache, R., E. Martin Rodríguez, N. Bogdan, F. Sanz-Rodríguez, M. d. C. Iglesias de la Cruz, Á. Juarranz de la Fuente, F. Vetrone, D. Jaque, J. Garcia Solé, and J. A. Capobianco, 2012, High resolution fluorescence imaging of cancers using lanthanide ion-doped upconverting nanocrystals: Cancers, v. 4, p. 1067-1105.

Osiński, M. A., B. A. Akins, J. B. Plumley, A. C. Rivera, G. A. Smolyakov, J. M. Vargas, and N. J. Withers, 2015, Thermal neutron detectors based on gadolinium-containing nanoscintillators, United States Patent 9,116,246.

Patnaik, P., 2004, Dean's Analytical Chemistry Handbook, v. 1143, McGraw-Hill New York.

Hamamatsu, 2004, Characteristics and use of infrared detectors: Hamamatsu Photonics.

Quici, S., M. Cavazzini, G. Marzanni, G. Accorsi, N. Armaroli, B. Ventura, and F. Barigelletti, 2005, Visible and near-infrared intense luminescence from water-

soluble lanthanide [Tb (III), Eu (III), Sm (III), Dy (III), Pr (III), Ho (III), Yb (III), Nd (III), Er (III)] complexes: Inorganic Chemistry, v. 44, p. 529-537.

Ricci, E., and R. Hahn, 1965, Theory and experiment in rapid, sensitive helium-3 activation analysis. Helium-3 reactions as neutron sources: Analytical Chemistry, v. 37, p. 742-748.

Rivera, A. C., N. N. Glazener, N. C. Cook, B. A. Akins, L. M. Armijo, J. B. Plumley, N. J. Withers, K. Carpenter, G. A. Smolyakov, R. D. Busch and M. Osiński, 2014, Characterisation of potassium bromide loaded with dysprosium fluoride nanocrystals for neutron detection: International Journal of Nanotechnology, v. 11, p. 529-538.

Rivera, A. C., N. N. Glazener, N. C. Cook, B. A. Akins, J. B. Plumley, N. J. Withers, K. Carpenter, G. A. Smolyakov, R. D. Busch, and M. Osiński, 2011, "*Detection of thermal neutrons using gadolinium-oxide-based nanocrystals*", Chemical, Biological, Radiological, Nuclear, and Explosives (CBRNE) Sensing XII (A. W. Fountain, III and P. J. Gardner, Eds.), SPIE Defense, Security, and Sensing Symposium, Orlando, Florida, 25-29 April 2011, Proceedings of SPIE, Vol. 8018, Paper 80180F (12 pp.).

Sears, V. F., 1992, Neutron scattering lengths and cross sections: Neutron news, v. 3, p. 26-37.

Setua, S., D. Menon, A. Asok, S. Nair, and M. Koyakutty, 2010, Folate receptor targeted, rare-earth oxide nanocrystals for bi-modal fluorescence and magnetic imaging of cancer cells: Biomaterials, v. 31, p. 714-729.

Siegmund, O. H., J. V. Vallerga, A. Martin, B. Feller, M. Arif, D. S. Hussey, and D. L. Jacobson, 2007, A high spatial resolution event counting neutron detector using microchannel plates and cross delay line readout: Nuclear Instruments and Methods in Physics Research Section A: Accelerators, Spectrometers, Detectors and Associated Equipment, v. 579, p. 188-191.

Sonzongi, A., 2009, Nudat 2.5, http://www.nndc.bnl.gov/nudat2/, Brookhaven National Laboratory.

Stouwdam, J. W., and F. C. van Veggel, 2002, Near-infrared emission of redispersible Er^{3+}, Nd^{3+}, and Ho^{3+} doped LaF_3 nanoparticles: Nano Letters, v. 2, p. 733-737.

Van Loef, E., P. Dorenbos, C. Van Eijk, K. Krämer, and H. Güdel, 2002, Scintillation properties of LaBr 3: Ce 3+ crystals: fast, efficient and high-energy-resolution scintillators: Nuclear Instruments and Methods in Physics Research Section A: Accelerators, Spectrometers, Detectors and Associated Equipment, v. 486, p. 254-258.

Vernimmen, B., W. Dullaert, and S. Engelen, 2007, Schedule unreliability in liner shipping: origins and consequences for the hinterland supply chain: Maritime Economics & Logistics, v. 9, p. 193-213.

Wald, M. L., 2009, Shortage slows a program to detect nuclear bombs: The New York Times, v. 11, p. 23.

Wang, H., J. Yang, C. Zhang, and J. Lin, 2009, Synthesis and characterization of monodisperse spherical $SiO_2@RE_2O_3$ (RE = rare earth elements) and $SiO_2@Gd_2O_3:Ln^{3+}$ (Ln = Eu, Tb, Dy, Sm, Er, Ho) particles with core-shell structure: Journal of Solid State Chemistry, v. 182, p. 2716-2724.

Williams, D. B., and C. B. Carter, 1996, The Transmission Electron Microscope, Springer.

Withers, N. J., Y. Brandt, A. C. Rivera, L. M. Armijo, N. C. Cook, and M. Osinski, "*Effects of $La_{0.2}Ce_{0.6}Eu_{0.2}F_3$ nanoparticles capped with polyethylene glycol on human astrocytoma cells in vitro*", Colloidal Nanocrystals for Biomedical Applications VII (W. J. Parak, M. Osiński, and K. Yamamoto, Eds.), SPIE International Symposium on Biomedical Optics BiOS 2012, San Francisco, California, 21-23 January 2012, Proceedings of SPIE, Vol. 8232, Paper 82320R (9 pp.).

Withers, N. J., N. N. Glazener, J. B. Plumley, B. A. Akins, A. C. Rivera, N. C. Cook, G. A. Smolyakov, G. S. Timmins, and M. Osiński, "*Locally increased mortality of gamma-irradiated cells in presence of lanthanide-halide nanoparticles*", Colloidal Quantum Dots/Nanocrystals for Biomedical Applications VI (W. J. Parak, K. Yamamoto, and M. Osiński, Eds.), SPIE International Symposium on Biomedical Optics BiOS 2011, San Francisco, California, 22-24 January 2011, Proceedings of SPIE, Vol. 7909, Paper 7909-0L (12 pp.).

Withers, N. J., N. N. Glazener, A. C. Rivera, B. A. Akins, L. M. Armijo, J. B. Plumley, N. C. Cook, J. M. Sugar, R. Chan, and Y. I. Brandt, 2013, Effects of La0. 2Ce0. 6Eu0. 2F3 nanocrystals capped with polyethylene glycol on human pancreatic cancer cells in vitro: SPIE International Symposium on Biomedical Optics BiOS 2012, San Francisco, California, 21-23 January 2013, Proceedings of SPIE, Vol. 85951O Paper 85951O (9 pp).

Withers, N. J., J. B. Plumley, B. A. Akins, A. C. Rivera, G. Medina, G. A. Smolyakov, G. S. Timmins, and M. Osinski, Radiation sensitivity enhancement in cells using high-Z nanoparticles: SPIE International Symposium on Biomedical Optics BiOS 2012, San Francisco, California, 21-23 January 2012, Proceedings of SPIE, Vol. 8232, Paper 82320R (9 pp.).p. 75750Z-75750Z-10.

Woolf, A. F., 2014, The New START Treaty: Central Limits and Key Provisions.

Xiao, Q., X. Zheng, W. Bu, W. Ge, S. Zhang, F. Chen, H. Xing, Q. Ren, W. Fan, and K. Zhao, 2013, A core/satellite multifunctional nanotheranostic for in vivo imaging and tumor eradication by radiation/photothermal synergistic therapy: Journal of the American Chemical Society, v. 135, p. 13041-13048.

Yang, J., C. Li, Z. Quan, C. Zhang, P. Yang, Y. Li, C. Yu, and J. Lin, 2008, Self-Assembled 3D Flowerlike Lu_2O_3 and Lu_2O_3:Ln^{3+} (Ln= Eu, Tb, Dy, Pr, Sm, Er, Ho, Tm) Microarchitectures: Ethylene Glycol-Mediated Hydrothermal Synthesis and Luminescent Properties: The Journal of Physical Chemistry C, v. 112, p. 12777-12785.

Yang, J.-S., J.-L. Kim, D.-y. Kim, and S.-Y. Chang, 2004, Development of a TL detector for neutron measurement by $CaSO_4$:Dy phosphors: Radiation Protection Dosimetry, v. 110, p. 301-304.

Zhou, J., Y. Sun, X. Du, L. Xiong, H. Hu, and F. Li, 2010, Dual-modality in vivo imaging using rare-earth nanocrystals with near-infrared to near-infrared (NIR-to-NIR) upconversion luminescence and magnetic resonance properties: Biomaterials, v. 31, p. 3287-3295.

Publications

1. N. J. Withers, J. B. Plumley, N. D. Triño, K. Sankar, B. A. Akins, A. C. Rivera, G. A. Smolyakov, G. S. Timmins, and M. Osiński, "*Scintillating-nanoparticle-induced enhancement of absorbed radiation dose*", Colloidal Quantum Dots for Biomedical Applications IV (M. Osiński, T. M. Jovin, and K. Yamamoto, Eds.), SPIE International Symposium on Biomedical Optics BiOS 2009, San Jose, California, 24-26 January 2009, Proceedings of SPIE, Vol. 7189, Paper 718917 (8 pp.).

2. N. J. Withers, B. A. Akins, A. C. Rivera, J. B. Plumley, G. A. Smolyakov, and M. Osiński, "*Lead-iodide based nanoscintillators for detection of ionizing radiation*", Chemical, Biological, Radiological, Nuclear, and Explosives (CBRNE) Sensing X (A. W. Fountain, III and P. J. Gardner, Eds.), SPIE Defense, Security, and Sensing Symposium, Orlando, Florida, 14-16 April 2009, Proceedings of SPIE, Vol. 7304, Paper 73041N (12 pp.).

3. M. Osiński, K. Sankar, N. J. Withers, J. B. Plumley, A. C. Rivera, B. A. Akins, and G. A. Smolyakov, "*Lanthanide-halide-based nanoscintillators for portable radiological detectors (Invited Paper)*", Optics and Photonics in Global Homeland Security V and Biometric Technology for Human Identification VI (C. S. Halvorson, Š. O. Southern, B. V. K. V. Kumar, S. Prabhakar, and A. A. Ross, Eds.), SPIE Defense, Security, and Sensing Symposium, Orlando, Florida, 13-16 April 2009, Proceedings of SPIE, Vol. 7306, Paper 730617 (16 pp.).

4. N. J. Withers, K. Sankar, J. B. Plumley, B. A. Akins, T. A. Memon, A. C. Rivera, G. A. Smolyakov, and M. Osiński, "*Optimization of Ce content in $Ce_xLa_{1-x}F_3$ colloidal nanocrystals for gamma radiation detection*", Nuclear Radiation Detection Materials – 2009 (D. L. Perry, A. Burger, L. Franks, K. Yasuda, and M. Fiederle, Eds.), 2009 MRS Spring Meeting, San Francisco, California, 13-17 April 2009, MRS Symposium Proceedings, Vol. 1164, Paper L07-02 (6 pp.).

5. N. J. Withers, J. B. Plumley, B. A. Akins, A. C. Rivera, G. Medina, G. A. Smolyakov, G. S. Timmins, and M. Osiński, "*Radiation sensitivity enhancement in cells using high-Z nanoparticles*", Colloidal Quantum Dots for Biomedical Applications V (M. Osiński, W. J. Parak, T. M. Jovin, and K. Yamamoto, Eds.), SPIE International Symposium on Biomedical Optics BiOS 2010, San Francisco, California, 23-25 January 2010, Proceedings of SPIE, Vol. 7575, Paper 75750Z (10 pp.).

6. M. Osiński, J. B. Plumley, N. J. Withers, B. A. Akins, G. Medina, A. C. Rivera, and G. A. Smolyakov, "*Synthesis and characterization of lanthanide halide scintillating nanocrystals for gamma radiation detection*", Proceedings of the 2010 International Conference on Nanoscience and Nanotechnology ICONN 2010 (A. Dzurak, Ed.), Sydney, Australia, 22-26 February 2010, pp. 189-192.

7. J. B. Plumley, N. J. Withers, A. C. Rivera, B. A. Akins, J. M. Vargas, K. Carpenter, G. A. Smolyakov, R. D. Busch, and M. Osiński, "*Thermal neutron detectors based on gadolinium-containing lanthanide-halide nanoscintillators*", Chemical, Biological, Radiological, Nuclear, and Explosives (CBRNE) Sensing XI (A. W. Fountain, III and P. J. Gardner, Eds.), SPIE Defense, Security, and Sensing

Symposium, Orlando, Florida, 6-8 April 2010, Proceedings of SPIE, Vol. 7665, Paper 76651F (13 pp.).

8. B. A. Akins, G. Medina, T. A. Memon, A. C. Rivera, G. A. Smolyakov, and M. Osiński, "*Nanophosphors based on CdSe/ZnS and CdSe/SiO_2 colloidal quantum dots for daylight-quality white LEDs*", Conference Digest, Thirtieth Annual Conference on Lasers and Electro-Optics CLEO 2010, San Jose, California, 16-21 May 2010, Paper CTuNN7.

9. N. J. Withers, N. N. Glazener, J. B. Plumley, B. A. Akins, A. C. Rivera, N. C. Cook, G. A. Smolyakov, G. S. Timmins, and M. Osiński, "*Locally increased mortality of gamma-irradiated cells in presence of lanthanide-halide nanoparticles*", Colloidal Quantum Dots/Nanocrystals for Biomedical Applications VI (W. J. Parak, K. Yamamoto, and M. Osiński, Eds.), SPIE International Symposium on Biomedical Optics BiOS 2011, San Francisco, California, 22-24 January 2011, Proceedings of SPIE, Vol. 7909, Paper 7909-0L (12 pp.).

10. M. Osiński, Y. Brandt, J. M. Vargas, J. B. Plumley, S. R. Maestas, A. C. Rivera, N. C. Cook, N. J. Withers, G. A. Smolyakov, N. L. Adolphi, S. L. McGill, I. El-Sherbiny, and H. D. C. Smyth, "*Multifunctional nanoparticles for lung delivery of drugs (Invited Paper)*", Fifth International Conference on Advanced Materials and Nanotechnology AMN-5, Wellington, New Zealand, 7-11 February 2011.

11. J. M. Vargas, A. A. McBride, J. B. Plumley, Y. Fichou, T. A. Memon, V. Shah, N. Cook, B. A. Akins, A. C. Rivera, G. A. Smolyakov, J. R. O'Brien, N. L. Adolphi, H. D. C. Smyth, and M. Osiński, "*Synthesis and characterization of core/shell*

Fe_3O_4/ZnSe fluorescent magnetic nanoparticles", Journal of Applied Physics **109** (#7), Art. 07B536 (3 pp.), April 2011.

12. A. C. Rivera, N. N. Glazener, N. C. Cook, B. A. Akins, J. B. Plumley, N. J. Withers, K. Carpenter, G. A. Smolyakov, R. D. Busch, and M. Osiński, "*Detection of thermal neutrons using gadolinium-oxide-based nanocrystals*", Chemical, Biological, Radiological, Nuclear, and Explosives (CBRNE) Sensing XII (A. W. Fountain, III and P. J. Gardner, Eds.), SPIE Defense, Security, and Sensing Symposium, Orlando, Florida, 25-29 April 2011, Proceedings of SPIE, Vol. 8018, Paper 80180F (12 pp.).

13. A. C. Rivera, N. C. Cook, N. N. Glazener, N. J. Withers, J. B. Plumley, B. A. Akins, G. A. Smolyakov, R. D. Busch, and M. Osiński, "*Dysprosium-containing nanocrystals for thermal neutron detection*", Nuclear Radiation Detection Materials (A. Burger, M. Fiederle, L. Franks, K. Lynn, D. L. Perry, and K. Yasuda, Eds.), 2011 MRS Spring Meeting, San Francisco, California, 26-28 April 2011, MRS Symposium Proceedings, Vol. 1341, Paper U9.2 (6 pp.).

14. M. Osiński, B. A. Akins, J. B. Plumley, A. C. Rivera, N. C. Cook, A. Agarwal, and G. A. Smolyakov, "*High-temperature nanophosphors for white-light-emitting diodes(Invited Paper)*", Proceedings of the 16thOpto-Electronics and Communications Conference OECC 2011, Kaohsiung, Taiwan, 4-8 July 2011 (4 pp.).

15. M. Osiński, L. M. Armijo, Y. Brandt, S. R. Maestas, A. C. Rivera, N. C. Cook, J. B. Plumley, B. A. Akins, G. A. Smolyakov, N. L. Adolphi, D. L. Huber, S. L. McGill, L. Gong, and H. D. C. Smyth, "*Multifunctional nanoparticles for drug delivery in cystic fibrosis (Invited Paper)*", Zing Nanomaterials Conference, Xcaret, Quintana Roo, Mexico, 28 November – 2 December 2011.

16. L. M. Armijo, Y. Brandt, D. Mathew, S. Yadav, S. Maestas, A. C. Rivera, N. C. Cook, N. J. Withers, G. A. Smolyakov, N. L. Adolphi, T. C. Monson, H. D. C. Smyth, and M. Osiński, "*Iron oxide nanocrystals for magnetic hyperthermia applications*", Technical Digest, Zing Nanomaterials Conference, Xcaret, Quintana Roo, Mexico, 28 November – 2 December 2011, p. 56.

17. A. C. Rivera, N. N. Glazener,N. C. Cook, L. M. Armijo, J. B. Plumley, B. A. Akins, K. Carpenter, G. A. Smolyakov, R. D. Busch, and M. Osiński, "*Dysprosium-containing nanocrystals for use as a neutron detector in a solvent suspension*", Technical Digest, Zing Nanomaterials Conference, Xcaret, Quintana Roo, Mexico, 28 November – 2 December 2011, p. 62.

18. L. M. Armijo, Y. I. Brandt, N. J. Withers, J. B. Plumley, N. C. Cook, A. C. Rivera, S. Yadav, G. A. Smolyakov, T. Monson, D. L. Huber, H. D. C. Smyth, and M. Osiński, "*Multifunctional superparamagnetic nanocrystals for imaging and targeted drug delivery to the lung*", Colloidal Nanocrystals for Biomedical Applications VII (W. J. Parak, M. Osiński, and K. Yamamoto, Eds.), SPIE International Symposium on Biomedical Optics BiOS 2012, San Francisco, California, 21-23 January 2012, Proceedings of SPIE, Vol. 8232, Paper 82320M (11 pp.).

19. N. J. Withers, Y. I. Brandt, A. C. Rivera, N. C. Cook, L. M. Armijo, G. A. Smolyakov, and M. Osiński, "*Effects of $La_{0.2}Ce_{0.6}Eu_{0.2}F_3$ nanoparticles capped with polyethylene glycol on human astrocytoma cells in vitro*", Colloidal Nanocrystals for Biomedical Applications VII (W. J. Parak, M. Osiński, and K. Yamamoto, Eds.), SPIE International Symposium on Biomedical Optics BiOS 2012, San Francisco, California, 21-23 January 2012, Proceedings of SPIE, Vol. 8232, Paper 82320R (9 pp.).

20. A. C. Rivera, N. N. Glazener, N. C. Cook, S. Maestas, B. A. Akins, L. M. Armijo, J. B. Plumley, N. J. Withers, K. Carpenter, G. A. Smolyakov, R. D. Busch, and M. Osiński, "*Thermal neutron detection with PMMA nanocomposites containing dysprosium fluoride nanocrystals*", Chemical, Biological, Radiological, Nuclear, and Explosives (CBRNE) Sensing XIII (A. W. Fountain III, Ed.), SPIE Defense, Security, and Sensing Symposium, Baltimore, Maryland, 23-27 April 2012, Proceedings of SPIE, Vol. 8358, Paper 83581S (9 pp.).

21. B. A. Akins, A. C. Rivera, N. C. Cook, G. A. Smolyakov, and M. Osiński, "*ZnSe:Mn/ZnS high temperature nanophosphors with very high quantum efficiency for white LEDs*", Technical Digest, Thirty Second Annual Conference on Lasers and Electro-Optics CLEO 2012, San Jose, California, 1-6 May 2012, Paper CW1L.2.

22. L. M. Armijo, Y. I. Brandt, D. Mathew, S. Yadav, S. Maestas, A. C. Rivera, N. C. Cook, N. J. Withers, G. A. Smolyakov, N. L. Adolphi, T. C. Monson, D. L. Huber, H. D. C. Smyth, and M. Osiński, "*Iron oxide nanocrystals for magnetic hyperthermia applications*", Nanomaterials **2** (#2), pp. 134-146, 7 May 2012.

23. B. A. Akins, A. C. Rivera, J. B. Plumley, N. C. Cook, S. A. Ivanov, G. A. Smolyakov, and M. Osiński, "*Cadmium-free ZnSe:Mn/ZnS high temperature nanophosphors with record high quantum efficiency for white LED applications*", Technical Digest, 7th International Conference on Quantum Dots, Santa Fe, New Mexico, 13-18 May 2012, Paper Th-72.

24. N. C. Cook, A. C. Rivera, N. N. Glazener, B. A. Akins, L. M. Armijo, J. B. Plumley, N. J. Withers, K. Carpenter, G. A. Smolyakov, R. D. Busch, and M. Osiński, "*Polyvinyl toluene/Gd_2O_3:10%Ce scintillating nanocomposites for thermal neutron detection*", Technical Digest, 7th International Conference on Quantum Dots, Santa Fe, New Mexico, 13-18 May 2012, Paper Th-73.

25. L. M. Armijo, Y. I. Brandt, S. R. Maestas, A. C. Rivera, N. C. Cook, N. J. Withers, G. A. Smolyakov, N. L. Adolphi, T. C. Monson, D. L. Huber, H. D. C. Smyth, and M. Osiński, "*Multifunctional nanocrystals for drug delivery in cystic fibrosis*", Technical Digest, 7th International Conference on Quantum Dots, Santa Fe, New Mexico, 13-18 May 2012, Paper Th-74.

26. A. C. Rivera, N. N. Glazener,N. C. Cook, S. R. Maestas, B. A. Akins, L. M. Armijo, J. B. Plumley, N. J. Withers, K. Carpenter, G. A. Smolyakov, R. D. Busch, and M. Osiński, "*Thermal neutron detection with Gd_2O_3:10%Ce nanocrystals loaded into a polyvinyl toluene matrix*", IEEE Symposium on Radiation Measurements and Applications SORMA WEST 2012, Oakland, California, 14-17 May 2012.

27. L. M. Armijo, Y. I. Brandt, A. C. Rivera, N. C. Cook, J. B. Plumley, N. J. Withers, M. Kopciuch, G. A. Smolyakov, D. L. Huber, H. D. C. Smyth, and M. Osiński, "*Multifunctional superparamagnetic nanoparticles for enhanced drug transport in cystic fibrosis*", Nanosystems in Engineering and Medicine (S. H. Choi, J.-H. Choy, U. Lee, and V. K. Varadan, Eds.), Incheon, Korea, 10-12 September 2012, Proceedings of SPIE, Vol. 8548, Paper 85480E (12 pp).

28. L. M. Armijo, B. A. Akins, J. B. Plumley, A. C. Rivera, N. J. Withers, N. C. Cook, G. A. Smolyakov, D. L. Huber, H. D. C. Smyth, and M. Osiński, "*Highly efficient multifunctional MnSe/ZnSeS quantum dots for biomedical applications*", Colloidal Nanoparticles for Biomedical Applications VIII (W. J. Parak, M. Osiński, and K. Yamamoto, Eds.), SPIE International Symposium on Biomedical Optics BiOS 2013, San Francisco, California, 2-4 February 2013, Proceedings of SPIE, Vol. 8595, Paper 859517 (7 pp.).

29. Y. I. Brandt, L. M. Armijo, A. C. Rivera, J. B. Plumley, N. C. Cook, G. A. Smolyakov, H. D. C. Smyth, and M. Osiński, "*Effectiveness of tobramycin conjugated to iron oxide nanoparticles in treating infection in cystic fibrosis*", Colloidal Nanoparticles for Biomedical Applications VIII (W. J. Parak, M. Osiński, and K. Yamamoto, Eds.), SPIE International Symposium on Biomedical Optics BiOS 2013, San Francisco, California, 2-4 February 2013, Proceedings of SPIE, Vol. 8595, Paper 85951C (9 pp.).

30. N. J. Withers, N. N. Glazener, A. C. Rivera, B. A. Akins, L. M. Armijo, J. B. Plumley, N. C. Cook, J. M. Sugar, R. Chan, Y. I. Brandt, G. A. Smolyakov, P. H. Heintz, and M. Osiński, "*Effects of $La_{0.2}Ce_{0.6}Eu_{0.2}F_3$ nanocrystals capped with*

polyethylene glycol on human pancreatic cancer cells in vitro", Colloidal Nanoparticles for Biomedical Applications VIII (W. J. Parak, M. Osiński, and K. Yamamoto, Eds.), SPIE International Symposium on Biomedical Optics BiOS 2013, San Francisco, California, 2-4 February 2013, Proceedings of SPIE, Vol. 8595, Paper 85951O (9 pp.).

31. A. C. Rivera, N. N. Glazener,N. C. Cook, L. M. Armijo, J. B. Plumley, N. J. Withers, K. Carpenter, G. A. Smolyakov, R. D. Busch, and M. Osiński, "*Characterization of potassium bromide loaded with dysprosium fluoride nanocrystals for neutron detection*", Technical Digest, Sixth International Conference on Advanced Materials and Nanotechnology AMN-6, Auckland, New Zealand, 11-15 February 2013.

32. L. M. Armijo, A. C. Rivera, J. B. Plumley, N. C. Cook, S. Maestas, G. A. Smolyakov, T. C. Monson, D. L. Huber, and M. Osiński, "*Basic mechanisms involved in the magnetization reversal of magnetic single-domain nanoparticles*", Technical Digest, Sixth International Conference on Advanced Materials and Nanotechnology AMN-6, Auckland, New Zealand, 11-15 February 2013.

33. A. C. Rivera, N. N. Glazener, N. C. Cook, N. J. Withers, L. M. Armijo, D. A. Huang, J. B. Wright, I. Brener, K. Carpenter, R. D. Busch, G. A. Smolyakov, and M. Osiński, "*Synthesis and characterization of ytterbium-doped dysprosium fluoride nanocrystals for use as neutron detectors*", 21st Annual International Conference on Composites / Nano Engineering ICCE-21, Santa Cruz de Tenerife, Spain, July 21-27, 2013.

34. L. M. Armijo, M. Kopciuch, B. A. Akins, J. B. Plumley, N. J. Withers, A. C. Rivera, N. C. Cook, Y. I. Brandt, J. M. Baca, S. J. Wawrzyniec, G. A. Smolyakov, D. L. Huber, and M. Osiński, "*Low-toxicity magnetic nanomaterials for biomedical applications*", 21st Annual International Conference on Composites / Nano Engineering ICCE-21, Santa Cruz de Tenerife, Spain, July 21-27, 2013.

35. A. C. Rivera, N. N. Glazener, N. C. Cook, N. J. Withers, L. M. Armijo, J. Wright, I. Brener, K. Carpenter, R. D. Busch, G. A. Smolyakov, and M. Osiński, "*Thermal neutron detection using ytterbium-doped dysprosium fluoride nanocrystals*", Zing Nanomaterials 2013 Conference, 13-17 November 2013, Xcaret, Mexico.

36. L. M. Armijo, M. Kopciuch, Z. Olszówka, S. J. Wawrzyniec, A. C. Rivera, J. B. Plumley, N. C. Cook, Y. I. Brandt, D. L. Huber, G. A. Smolyakov, N. L. Adolphi, H. D. C. Smyth, and M. Osiński, "*Delivery of antibiotics coupled to iron oxide nanoparticles across the biofilm of mucoid Pseudonomas aeruginosa and investigation of their efficacy*", Colloidal Nanoparticles for Biomedical Applications IX (W. J. Parak, M. Osiński, and K. Yamamoto, Eds.), SPIE International Symposium on Biomedical Optics BiOS 2014, San Francisco, California, 1-3 February 2014, Proceedings of SPIE, Vol. 8955, Paper 89550I (12 pp.).

37. A. C. Rivera, N. N. Glazener,N. C. Cook, B. A. Akins, L. M. Armijo, J. B. Plumley, N. J. Withers, K. Carpenter, G. A. Smolyakov, R. D. Busch, and M. Osiński, "*Characterization of potassium bromide loaded with dysprosium fluoride*

nanocrystals for neutron detection", International Journal of Nanotechnology, vol. 11 (#5/6/7/8), pp. 529-538, April 2014.

38. M. Osiński, Y. I. Brandt, L. M. Armijo, J. B. Plumley, A. C. Rivera, N. C. Cook, G. A. Smolyakov, D. L. Huber, and H. D. C. Smyth, "*Superparamagnetic iron oxide nanoparticles conjugated to tobramycin for treating cystic fibrosis infections (Invited Paper)*", Technical Digest, 4th Zing Bionanomaterials Conference, Nerja, Spain, 6-9 April 2014, p. 53.

39. L. M. Armijo, P. Jain, A. Malagodi, F. Z. Fornelli, A. Hayat, A. C. Rivera, M. French, H. D. C. Smyth, and M. Osiński, "*Inhibition of bacterial growth by iron oxide nanoparticles with and without attached drug: Have we conquered the antibiotic resistance problem?*", Colloidal Nanoparticles for Biomedical Applications X (W. J. Parak, M. Osiński, and Xing-Jie Liang, Eds.), SPIE International Symposium on Biomedical Optics BiOS 2015, San Francisco, California, 7-9 February 2015, Proceedings of SPIE, Vol. 9338, Paper 1Q (11 pp.).

40. A. C. Rivera, L. M. Armijo, A. N. Edwards, N. M. Jones, E. J. Peterson, andM. Osiński, "*Green chemistry synthesis and characterization of lanthanide fluoride nanocrystals*", submitted to SpringerPlus.

41. A. C. Rivera, N. N. Glazener,N. C. Cook, S. R. Maestas, L. M. Armijo, J. B. Plumley, B. A. Akins, N. J. Withers, K. Carpenter, G. A. Smolyakov, R. D. Busch, and M. Osiński, "*Thermal neutron detection with dysprosium-containing nanocrystals suspended in toluene*", submitted to Nanomaterials.

Patent:

1. M. Osiński, B. A. Akins, A. C. Rivera, J. B. Plumley, G. A. Smolyakov, J. M. Vargas, and N. J. Withers "*Thermal neutron detectors based on gadolinium-containing nanoscintillators*", United States Provisional Patent Application 61/473,071 filed on 7 April 2011, United States Utility Patent Application 13/506,240 filed on 5 April 2012, allowed on 27 April 2015, United States Patent number 9,116,246, issued on 25 August 2015.